Generation and propagation of nonlinear internal waves in Massachusetts Bay

A. Scotti,[1] R. C. Beardsley,[2] and B. Butman[3]

[1] During the summer, nonlinear internal waves (NLIWs) are commonly observed propagating in Massachusetts Bay. The topography of the area is unique in the sense that the generation area (over Stellwagen Bank) is only 25 km away from the shoaling area, and thus it represents an excellent natural laboratory to study the life cycle of NLIWs. To assist in the interpretation of the data collected during the 1998 Massachusetts Bay Internal Wave Experiment (MBIWE98), a fully nonlinear and nonhydrostatic model covering the generation/shoaling region was developed, to investigate the response of the system to the range of background and driving conditions observed. Simplified models were also used to elucidate the role of nonlinearity and dispersion in shaping the NLIW field. This paper concentrates on the generation process and the subsequent evolution in the basin. The model was found to reproduce well the range of propagation characteristics observed (arrival time, propagation speed, amplitude), and provided a coherent framework to interpret the observations. Comparison with a fully nonlinear hydrostatic model shows that during the generation and initial evolution of the waves as they move away from Stellwagen Bank, dispersive effects play a negligible role. Thus the problem can be well understood considering the geometry of the characteristics along which the Riemann invariants of the hydrostatic problem propagate. Dispersion plays a role only during the evolution of the undular bore in the middle of Stellwagen Basin. The consequences for modeling NLIWs within hydrostatic models are briefly discussed at the end.

1. Introduction

[2] Nonlinear internal waves (NLIWs) have emerged in the past 30 years as a prominent feature of many shelf and coastal areas around the world. Already at the end of the 1960s, *Ziegenbein* [1969] and *Halpern* [1971a] reported the existence of high-frequency, large-amplitude tidally generated internal waves in the Strait of Gibraltar and in Massachusetts Bay. Such waves have been observed, among other places, on the New England shelf [*Colosi et al.*, 2001], on the Malin shelf [*Small et al.*, 1999; *Small*, 2003], in the Celtic Sea [*Holt and Thorpe*, 1997], near the Oregon coast [*Trevorrow*, 1998], in the East and South China Seas [*Ramp et al.*, 2004], in the Bay of Biscay [*New and Pingree*, 1992], in the Strait of Messina [*Brandt et al.*, 1996], in the Sulu Sea [*Apel et al.*, 1985], on the Scotian shelf [*Sandstrom and Elliot*, 1984], in the Gulf of California [*Fu and Holt*, 1984], in the New York Bight [*Liu*, 1988] and in the Andaman Sea [*Osborne and Burch*, 1980], using in situ observations as well as remote sensing techniques [*Apel et al.*, 1995]. For a comprehensive catalog of observations, the reader is referred to *Jackson* [2004]. Aside from their obvious physical interest, NLIWs impact several areas of coastal oceanography through enhanced mixing and transport [*MacKinnon and Gregg*, 2003; *Leichter et al.*, 2003; *Moum et al.*, 2003], biological oceanography by redistributing plankton [*Pineda*, 1999; *Helfrich and Pineda*, 2003; *Scotti and Pineda*, 2007], and geological oceanography by suspending and transporting sediments [*Bogucki et al.*, 1997; *Butman et al.*, 2006]. For this reason, much research has been devoted to modeling NLIWs [*Helfrich and Melville*, 2006].

[3] Of the three stages of the life of NLIWs, generation, propagation and dissipation/shoaling, the issue of propagation is probably the best understood at present. Using the amplitude of the wave and the wavenumber relative to an appropriate depth as parameters, several sets of equations can be derived from the Euler equations (neglecting viscosity) representing different regimes (shallow versus deep water, small amplitude versus large amplitude, etc. [see, e.g., *Whitham*, 1974; *Choi and Camassa*, 1999; *Ostrovsky and Grue*, 2003]). These simplified equations extend from the original inviscid Korteweg-deVries (KdV) equation [*Korteweg and de Vries*, 1895], which is amenable to analytic solutions that have provided much insight into the behavior of nonlinear IWs, to the extended KdV

[1] Department of Marine Sciences, University of North Carolina, Chapel Hill, North Carolina, USA.
[2] Department of Physical Oceanography, Woods Hole Oceanography Institution, Woods Hole, Massachusetts, USA.
[3] U.S. Geological Survey, Woods Hole, Massachusetts, USA.
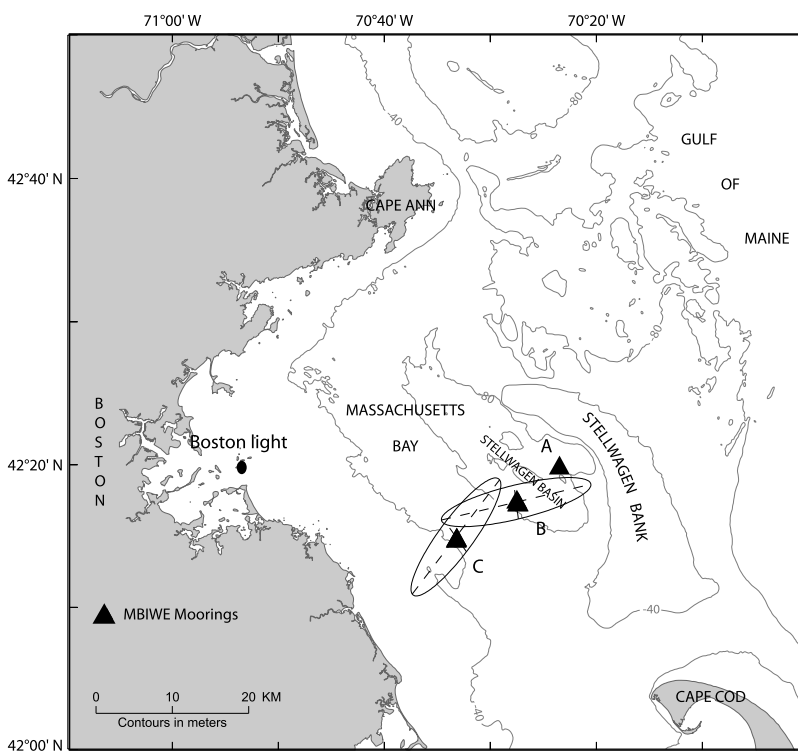
Figure 1. Map of the Massachusetts Bay/Stellwagen Bank area. The triangles marked A, B, and C mark the positions of the moorings deployed during MBIWE98. The plot also shows the barotropic M2 tidal ellipses at stations B and C.

equation, which includes some effects of rotation, depth and stratification change, and friction, at the cost of forgoing analytical solutions [*Holloway et al.*, 1999], to the Choi and Camassa equation [*Choi and Camassa*, 1999] describing the motion of long-wavelength, large waves in a two-layer system. Generation mechanisms for NLIWs are more complex and subject to fewer investigations. In many locations, the timing and periodicity of the waves strongly suggest a tidal origin, where the barotropic tidal flow over some topographic feature (such as a sill or shelf break) injects energy into the wave field at regular intervals. The exact details of this generation process are often complicated by other factors, such as areas where the flow becomes supercritical [*Grimshaw and Smyth*, 1986], local instabilities, 3D effects and so on [*Farmer and Armi*, 1998, 1999].

[4] Parallel to the analytical approach, numerical solutions of the Euler (or Navier-Stokes equations) have become commonplace [*Hibiya*, 1988; *Lamb*, 1994; *Vlasenko and Hutter*, 2002]. For reasons discussed in more details later, the only approximation is that the flow be two-dimensional. The latter models offer a more complete description of NLIWs than traditional analytical models, and have been used for a variety of process-oriented studies of NLIWs [*Lamb*, 1997; *Vlasenko and Hutter*, 2002]. With few exceptions [*Cummins*, 2000; *Bourgalt et al.*, 2005], advanced models have not been used to consider NLIWs in realistic settings, and when done, only a limited part of the cycle has been considered. This situation is in part due to the fact that in most places where NLIWs are observed, putative generation and shoaling/dissipation areas are far apart,

which poses a severe strain on the computational resources. Massachusetts Bay represents an exception to this rule, as generation and dissipation areas are only 25 km apart, equivalent to about 100 times the wavelength of the high-frequency nonlinear internal waves observed in the area. Moreover, NLIWs are highly predictable in the summer, and thus represents an excellent natural lab to study the life cycle of NLIWs.

[5] In spite of this privileged condition, no serious attempt has been made to model the NLIW field in the area, with the exception of the pioneering work of *Lee and Beardsley* [1974] and *Hibiya* [1988], who however considered only the generation process over Stellwagen Bank. In this paper, we model NLIWs in this area using a suite of models, ranging from a two-layer hydrostatic model to a fully nonhydrostatic and nonlinear model, and compare the results with observations gathered in the area during the 1998 Massachusetts Bay Internal Wave Experiment (MBIWE98) [*Butman et al.*, 2004]. The focus is on the initial generation and evolution of NLIWs as they propagate westward from Stellwagen Bank (Figure 1). The interaction with the shoaling bottom will be covered in a forthcoming paper. The aim here is twofold: We want to understand the relative role of nonlinearity and dispersion in the evolution of NLIWs, and we want to present a modeling framework to interpret NLIWs observations in the area, to benefit future field work.

[6] The main result is that nonlinearity plays a fundamental role during the generation and shoaling process. Initialized with realistic values of stratification, the fully nonlinear and nonhydrostatic model provides a good

description of the features observed in the Massachusetts Bay NLIW field during MBIWE98. During the propagation phase, dispersion is responsible for the generation of high-frequency internal waves trailing the leading edge of the nonlinear internal tide. However, we show that a hydrostatic simulation captures the large-scale properties of the nonlinear internal tide (i.e., speed of propagation and amplitude), provided sufficient dissipation is allowed. This result opens up the tantalizing possibility to devise suitable parameterizations for hydrostatic models to be used when internal undular bores (solibores) are expected.

2. NLIWs in Massachusetts Bay

[7] Massachusetts Bay (Mass Bay) lies between Stellwagen Bank to the east and the Massachusetts coast to the west (Figure 1). The bank has an asymmetrical profile; the western side drops rapidly (60 m over about 5 km) into Stellwagen Basin, while the eastern side presents a more gentle slope toward the Gulf of Maine. West of Stellwagen Basin, the bottom shoals to a shelf about 20 m deep and 10 km wide.

[8] During the summer, a seasonal pycnocline develops at about 20 m, separating the surface water warmed by solar radiation and slightly freshened by river runoff from the underlying colder and saltier water. The Brunt-Väisälä frequency in the pycnocline is about 0.04 s^{-1}. The surface tide in the Mass Bay/Boston Harbor system is essentially in phase everywhere, and is dominated by the semidiurnal components (mostly M2 with smaller but significant contributions from S2 and K2). Surface tidal excursions range from 3.6 m during spring tide to 1.8 m during neap tide [*Butman et al.*, 2004]. The semidiurnal tidal flow is characterized by narrow tidal ellipses with major axes aligned along the local across-isobath direction (Figure 1).

[9] The existence of NLIWs propagating across Mass Bay is well established. *Halpern* [1971a, 1971b] first observed and described large-amplitude, high-frequency internal waves of depression propagating on the shallow seasonal pycnocline toward the west/southwest across Stellwagen Basin. A more comprehensive set of observations was collected by *Haury et al.* [1979, 1983], who advanced the hypothesis that the packets are formed when the lee wave on the eastern side of Stellwagen Bank generated by the ebbing tide is released. The flow over the bank was described as subcritical relative to the internal long-wave speed. The latter observation was challenged by *Chereskin* [1983], who reported a supercritical flow over the bank during most of the ebbing phase. Chereskin also mapped acoustically the flow, and showed the existence of a broad depression in the pycnocline, extending about 5 km eastward from the crest of the bank during the ebb phase. Later *Trask and Briscoe* [1983] used Synthetic Aperture Radar (SAR) images to study the propagation of NLIWs in Mass Bay. They were able to correlate features in the SAR images with the expected position of the waves based on the observations of *Haury et al.* [1979]. While the majority of the packets presented fairly straight fronts, a few packets seemed to emanate from a localized area, with curved fronts that may have been related to the curved crest of Stellwagen Bank. None of the investigators cited here reported evidence of eastward propagating IWs in Stellwagen Basin, suggesting

that the NLIWs observed moving westward across the bay were dissipated near the coast with no appreciable reflection.

[10] The data referred to in this paper were collected during the 1998 USGS-WHOI joint Massachusetts Bay Internal Wave Experiment (MBIWE98). Data were acquired at three heavily instrumented sites spanning the bay during the summer of 1998 (Figure 1), as well as during hydrographic cruises conducted during the same period. For details on the deployment, the reader is referred to *Butman et al.* [2004, 2006].

3. Nonlinear Internal Waves Models

[11] Theoretical treatment of NLIWs has almost always being confined to two-dimensional geometry (see, e.g., *Akylas and Davis* [2001] and references therein for a discussion of 3D effects). The advantages are obvious. Even models that, from the onset, are solved numerically greatly benefit from this assumption. Indeed, the horizontal scale of NLIWs is usually much smaller than the typical scale of the topography. Unless adaptive grids are employed, three-dimensional fixed grids large enough to accommodate the topography would require an unmanageable number of grid points. In our case, the assumption of two-dimensionality is justified by the visual observations of *Halpern* [1971a, 1971b] and by the analysis of SAR images [*Trask and Briscoe*, 1983], which show that the waves have relatively straight fronts extending O(10 km). This is likely due to the geometry of Stellwagen Bank (Figure 1) as well as to the short distance traveled by the waves before the shoaling area.

[12] Within the 2D hypothesis, the traditional starting point to describe interfacial NLIWs has been to consider (1) the amplitude of the waves a small relatively to an appropriately defined depth scale H of the order of the mixed layer above the pycnocline (*Baines* [1995, p. 125] shows that within the two-layer assumption, $H = \sqrt{d_{10}d_{20}/(d_{10} + d_{20})}$, where d_{10} (d_{20}) is the depth of the upper (lower) layer) and (2) the horizontal scale Δ large relative to H. From the Euler equations, it is possible to derive a hierarchy of equations by expanding the solution in powers of a/H and H/Δ. At the lowest nontrivial order, the waves satisfy the Korteweg-de Vries (KdV) equation [*Korteweg and de Vries*, 1895], or one of its closely related equations, such as the Benjamin-Ono equation or the Joseph equation [*Ono*, 1975; *Joseph*, 1977; *Ablowitz and Segur*, 1981], all of which are analytically integrable. The solutions to these equations form the conceptual framework to understand the propagation of NLIWs. Similar equations can be derived for a continuously stratified fluid [see, e.g., *Benney*, 1966; *Liu and Benney*, 1981]. In this case, the fields are projected on a suitable base of modes, and equations are sought determining the evolution of the amplitude of the modes, in the assumption that mode-mode interaction can be neglected. The KdV formalism has been extended to cases where the bottom topography and/or other quantities change along the propagation direction, leading to the forced extended KdV equation (feKdV) [*Grimshaw and Smyth*, 1986; *Grimshaw et al.*, 1999]. Holloway and coworkers have used these tools to study the internal waves propagating on the northwestern Australian shelf with some degree of
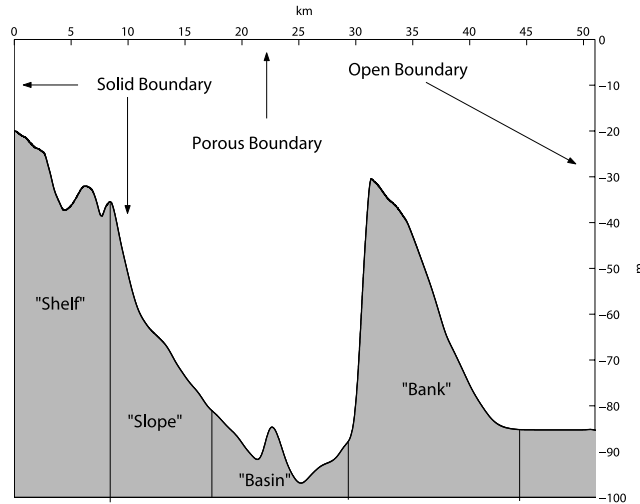
Figure 2. Schematic of the physical domain employed in the present study. The bottom depth follows the topography along the line connecting the moorings deployed during MBIWE98 up to $x = 45$ km, after which the depth is kept constant. Also indicated are the four regions (bank, basin, slope, and shelf) used to characterize the different regimes during the presentation of the results.

success [*Smyth and Holloway*, 1988; *Holloway et al.*, 1997, 1999].

[13] Despite its usefulness, the feKdV formalism presents several shortcomings, related to the underlying assumptions of (1) weak nonlinearity, (2) unidirectional wave propagation, and (3) modal decomposition. The energetics of NLIWs in Stellwagen Basin shows that the waves are strongly nonlinear [*Scotti et al.*, 2006], and thus points to the necessity of using fully nonlinear models.

[14] The tremendous increase in computational power made available to the scientific community in the past 15 years has made possible to develop models that solve directly the equations for the conservation of mass and momentum in a continuously stratified fluid. *Lamb* [1994] applied this strategy to study the generation of internal tides on the northern flank of Georges Bank, while *Hibiya* [1988] considered the generation of internal waves over Stellwagen Bank. In both cases, the equations were solved in the Boussinesq approximation. In this approach, the only explicit assumption is that the flow is 2D. Hibiya handled dissipation explicitly with a constant eddy viscosity model, while Lamb relied upon the numerical dissipation generated by the upwinding scheme. Our approach follows their approach closely. The main point of departure is in the numerical scheme used to solve the equations.

4. Model Description

[15] To model NLIWs in Massachussets Bay, we consider a 2D channel with variable bottom (Figure 2). The section between $x_1 = 0$ and $x_2 = 45$ km realistically models the bottom topography observed along the track connecting the mooring sites occupied during MBIWE98. East of x_2 the model topography is flat. We assume that the flow is governed by the two-dimensional equations for conservation of mass and momentum, using the Boussinesq approxima-

tion, and we fix a frame of reference (x, z) with x positive in the offshore direction, z positive upward in the vertical direction. The flow occupies the region $h(x) \leq z \leq D$, $0 \leq x \leq L$ (Figure 2). The channel is open on the eastern side (right), and closed on the western side.

[16] We write the total density as the sum of a steady part plus a perturbation term $\rho = \rho_0 + \overline{\rho}(z) + \rho'(x, z, t)$, and we solve for ρ'. If we introduce a stream function ψ, such that

$$(u, w) = \left(\frac{\partial \psi}{\partial z}, -\frac{\partial \psi}{\partial x} \right), \tag{1}$$

and let $\omega = \partial w / \partial x - \partial u / \partial z$ be the vorticity in the direction normal to the plane of the flow, the governing equations can be written as

$$\frac{\partial \rho'}{\partial t} - J(\psi, \rho') = J(\psi, \overline{\rho}), \tag{2}$$

$$\frac{\partial \omega}{\partial t} - J(\psi, \omega) = -g \frac{\partial \rho'}{\partial x}, \tag{3}$$

$$\omega = -\nabla^2 \psi, \tag{4}$$

where $J(\cdot, \cdot)$ denotes the Jacobian operator

$$J(f, g) = \frac{\partial f}{\partial x} \frac{\partial g}{\partial z} - \frac{\partial f}{\partial z} \frac{\partial g}{\partial x}. \tag{5}$$

[17] The flow is forced by prescribing the tidal flux on the eastern boundary. Because of the no-flux condition on the bottom and western boundaries, mass conservation requires a flux across the upper lid. Mathematically, this translates into the following boundary conditions for ψ

$$\begin{cases} \psi(0, z) = 0, \\ \psi(x, h(x)) = 0, \\ \psi(x, D) = Q(t) \frac{x}{L}, \\ \psi(L, z) = Q(t) \frac{z}{h(L)}. \end{cases} \tag{6}$$

[18] With this choice of boundary conditions, the barotropic tidal flow goes from being maximum at the eastern side to zero as we approach the shore. The inflow conditions for ρ' and ω are set by the spectral representation employed. On the eastern and western vertical boundaries we have $\partial \rho' / \partial x = 0$ and $\omega = 0$. The conditions along the vertical walls are clearly artificial, and will cause partial reflection of waves coming from the interior. To minimize the effect, we introduce a "sponge" layer near the eastern and western boundary that gradually dissipates the incoming waves. On the upper and lower surface $\rho' = 0$ and $\omega = 0$.

[19] The internal Rossby radius of deformation, based on the observed stratification, is minimum at the crest of the bank, being of the order of 2 km and maximum in the middle of the basin, about 4 km. In both areas, the radius is much larger than the wavelength of the observed waves, and the travel time from generation to shoaling is too short for resonance with Poincaré waves to occur [*Helfrich*, 2007]. Thus we neglect rotation. (However, given the strongly
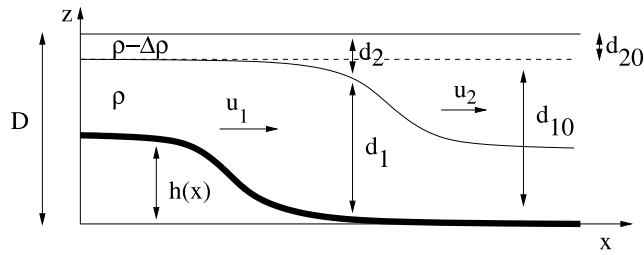
Figure 3. Notation used for the two-layer model. Here $d_{10,20}$ are the undisturbed depths away from the topography, $d_{1,2}$ are the actual depths, and $u_{1,2}$ are the depth-integrated velocities. The displacement is defined as $\eta = d_2 - d_{20} = d_1 - (d_{10} - h)$.

nonlinearity of these waves, both in the basin as well as in the shoaling region, the potential for tidal rectification cannot be completely ruled out.)

4.1. Numerical Discretization and Hydrostatic Limit

[20] It is well known that the main features of nonlinear waves are controlled by the interplay of nonlinear effects that steepen wavefronts vs. dispersive effects [*Ablowitz and Segur*, 1981]. Hence it is important to consider a numerical method that minimizes the error introduced in the computation of derivatives. We use a spectral discretization, employing a sine/cosine basis on collocation points, using the 2/3 rule to de-alias the nonlinear term [*Canuto et al.*, 1987]. The physical domain is mapped by means of a conformal map to a rectangular domain [*Fornberg*, 1984]. Time is advanced using a compact second-order Runge-Kutta scheme.

[21] The numerical code was validated at several levels. The overall correctness of the implementation, as well the convergence property of the scheme, was tested using monochromatic waves with constant stratification (which are exact solutions [*Lamb*, 2007]) and KdV solutions in the weakly nonlinear limit. The treatment of the variable bottom topography was verified reproducing results available in the literature, such as the simulations of *Lamb* [1994] of a stratified flow across a bank edge.

[22] The model accounts for nonlinear and dispersive (i.e., nonhydrostatic) effects. However, the latter effect is important only at small scales (see, e.g., the discussion by *Marshall et al.* [1997]). Conversely, the dynamics at large scales (i.e., in the long wavelength limit) is effectively hydrostatic, even when described by equations (2)–(4) above. Because of the spectral nature of the discretization, it is possible to run the model on a coarse grid without incurring significant numerical diffusion. Thus it is possible to study the effect of dispersion by simply varying the

smallest wavelength allowed in the model. To prevent spurious energy from accumulating at the smallest resolved scale (owing to the nonlinear terms), we introduce a Gaussian filter in Fourier space given by

$$G(k) = e^{-(k/k_c)^2/12}, \qquad (7)$$

applied to the density and vorticity fields once every buoyancy period. In the nondispersive case, the cutoff wavelength corresponding to k_c was set at 150 m (roughly the wavelength of the observed NLIWs), while in the dispersive case, it was set at 10 m. The latter value was chosen on the basis of experiments done with sech^2 pulses on a pycnocline, where we found that the minimum number of collocation points per wavelength necessary to achieve convergence was of the order of 10.

4.2. Simplified Models

[23] Nonlinearity and dispersion are the two physical mechanisms controlling the evolution of NLIWs. While it is possible to operate the model described above in such a way to emphasize one or the other, it is also instructive to consider two simplified models, one fully nonlinear but hydrostatic, the other weakly nonlinear and weakly nonhydrostatic. For the former, we consider a simple two-layer model (Figure 3). In the longwave, Boussinesq limit, conservation of mass and momentum can be rewritten in terms of the interfacial displacement η and baroclinic velocity $v = u_1 - u_2$ as

$$\frac{\partial \eta}{\partial t} + \frac{\partial}{\partial x}\left[\frac{d_2(d_1 v - Q)}{D - h}\right] = 0,$$
$$\frac{\partial v}{\partial t} + \frac{\partial}{\partial x}\left[g'\eta + \frac{(d_2 - d_1)v^2 + 2Qv}{D - h}\right] = 0, \qquad (8)$$

where Q is the barotropic, time-dependent flow-rate, $g' = g\Delta\rho/\rho$ the reduced gravity and d_1 and d_2 the thickness of the lower and upper layer respectively [*Baines*, 1995, chapter 3]. The advantage of this model is that when recast in terms of Riemann invariants, it allows a clean geometric interpretation of the physics. For the case when dispersion and nonlinearity are both important, we consider the KdV equation written in terms of the amplitude of the mode 1 wave η [see, e.g., *Liu and Benney*, 1981].

$$\frac{\partial \eta}{\partial t} + c_0 \frac{\partial}{\partial x}\left(\eta + \frac{\alpha}{2}\eta^2 + \beta\frac{\partial^2 \eta}{\partial x^2}\right) = 0, \qquad (9)$$

where α, β and c_0 are function of the background stratification and are defined in Appendix A. In this case

Table 1. Parameters Used for Computing Stratification in the Three Cases Considered

	a (σ_t)	b	c, m	d	f	Pycnocline Depth, m
Standard	3.55	7.17	16	0.37	3.6	10
Shallow	2.25	11.33	10	0.37	3.6	6
Deep	5.833	4.385	24	0.40	3.0	16.5

Table 2. Maximum Value of the Barotropic Current[a]

	Midbasin, m/s	Stellwagen Bank, m/s
Mean	0.13	0.52
Spring	0.16	0.65
Neap	0.10	0.39

[a]In the middle of Stellwagen Basin the values are based on observations. Over Stellwagen Bank the values are deduced assuming constant transport.
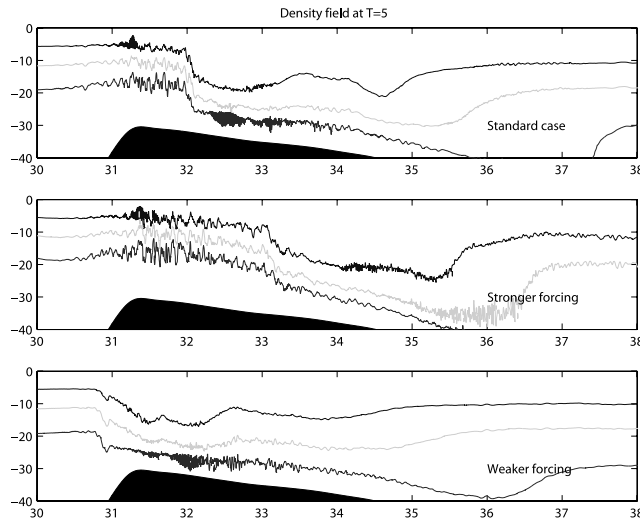
Figure 4. Density field 5 hours after beginning of ebb tide during (top) mean, (middle) spring, and (bottom) neap tide. The isolines contoured correspond to $\sigma_t = 22.5$, 23.5 and 24.5. Horizontal distances are in kilometers, and depths are in meters.

as well analytical solutions are possible, which help shedding light on the relevant physics.

4.3. Stratification, Forcing, and Initial Conditions

4.3.1. Stratification

[24] The stratification was modeled using the following profile,

$$\overline{\rho} = \begin{cases} a\big(b - e^{z/c+0.3125}\big) & \text{if } z/c \leq -1, \\ a\big(b - e^{z/c+0.3125} + d(z/c+1)^f\big) & \text{if } -1 \leq z/c \leq 0. \end{cases} \quad (10)$$

With the appropriate choice of the parameters (Table 1, standard case), this profile fits reasonably well the stratification measured in the middle of Stellwagen Basin during MBIWE98. To study the effects of the observed heaving of the pycnocline during the month-long deployment, we considered three cases with the same value for the maximum Brunt-Väisälä frequency fixed at $N_{max} = 0.037$ s^{-1}, but with different pycnocline depths. Table 1 lists the parameters used in the three cases.

4.3.2. Forcing

[25] *Hibiya* [1988] used an asymmetric tidal forcing in his study of the generation of internal tides over Stellwagen Bank, with the amplitude of the flood phase smaller relative to the ebb phase, based on the measurements reported by *Chereskin* [1983] over the bank. On the other hand, the measurements taken during MBIWE98 in Stellwagen Basin (west of the bank) indicate a fairly sinusoidal barotropic tide. In our model, we used the values measured in the basin. Because of continuity, the tide over the bank is sinusoidal as well. Some of the distortion measured by Chereskin over the bank might be due to undersampling a current with a profile that changes between flood and ebb. In any case, it is the ebb tide which is responsible for the

generation of the waves that propagate in the basin, thus the details of the flood phase are likely to play a minor role.

[26] We chose a sinusoidal forcing, with a period of 12.42 hours, and three amplitudes, corresponding to neap, mean and spring tide conditions respectively. Table 2 lists the amplitude of the barotropic tide in the middle of Stellwagen Basin and above Stellwagen Bank that was used. The values match the observed currents in Mass Bay.

4.3.3. Initial Conditions and Runs

[27] All simulations started at the beginning of the ebb phase with the fluid at rest. Each simulation was run for enough time to observe the complete life of at least two packets. The second packet was used to gauge the sensitivity of the process to the initial condition, which was found minimal. Out of the nine possible combinations of stratification and forcing, we selected six cases. Three cases with the forcing fixed at the mean level and changing stratification, and three cases keeping the stratification constant (using the observed value) and changing forcing intensity. In the following, we use the term standard to refer to the simulation done with mean forcing and observed stratification. Also, for convenience, time is expressed in terms of "hours" defined as $T/12$, where T is the period of the M2 tide (12.42 real hours).

5. Evolution of the Internal Wave Field in Massachusetts Bay

5.1. Generation

[28] In Figures 4 and 5, we show the density field over the bank at the end of the ebb phase, 1 hour before slack. At this time a depression is visible in the pycnocline, bounded to the west by a quasisteady bore-like wave at $x = 32$ km and extending eastward about 5 km. The spatial distribution of isopycnals is in excellent agreement with the acoustic
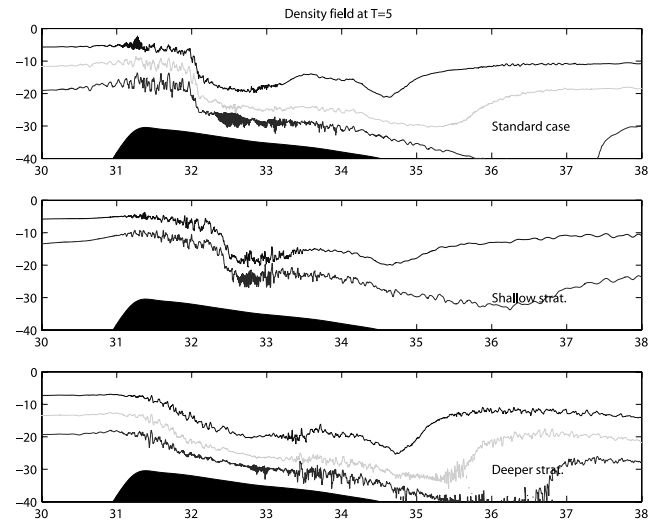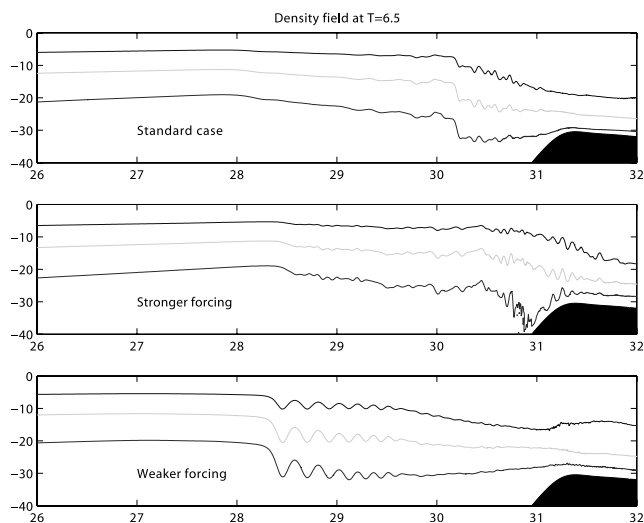

Figure 5. Density field 5 hours after beginning of the ebb tide, with (top) mean stratification, (middle) shallower and (bottom) deeper pycnocline. In the shallower case, the isolines contoured are for $\sigma_t = 23$ and 24, while for the deeper pycnocline, they are $\sigma_t = 20.5$, 21.5 and 22.5. Horizontal distances are in kilometers, and depths are in meters.
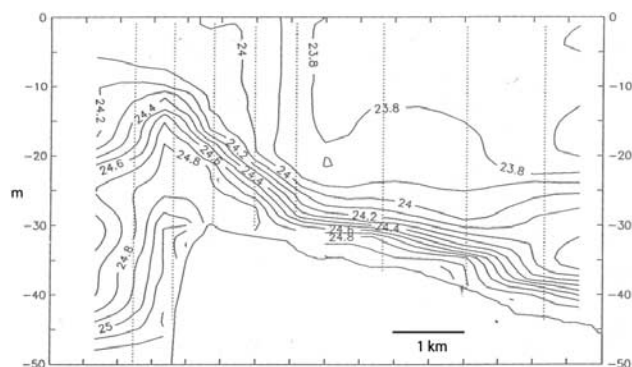
Figure 6. Density field measured over Stellwagen Bank on 30 September 1988 (R. Geyer and E. Terray, personal communication, 2006). The vertical dotted lines show the position of the CTD casts. The time is shortly before the end of ebb.

observations of *Chereskin* [1983] and with CTD measurements taken along the crest of the sill during the same phase of the tide (Figure 6). Along the depression, the current is bottom intensified, where the speed exceeds 70 cm/s. The depression originally develops over the crest of the bank, and it is slowly advected downstream, even after the ebb tide reaches its maximum intensity at $t = 3$. At the same time, the depression widens, reaching its widest extension around $t = 4.5$, when it begins to backtrack. Both upstream and downstream of the waves small-scale instabilities develop [*Pawlack and Armi*, 1998]. Above the depression the pool of water is almost stagnant, so that the configuration is similar to the one observed during downslope wind storms [*Smith*, 1985]. On the upstream (west) side of the bore-like wave, the isopycnals are slightly raised, and effect that becomes more pronounced as the wave leaves the crest during the propagation phase.

[29] Different environmental conditions result in a qualitatively similar picture. The depression is advected further

Figure 7. Density field 6.5 hours after beginning of ebbing tide during (top) mean, (middle) spring, and (bottom) neap tide. Isolines are as in Figure 4.
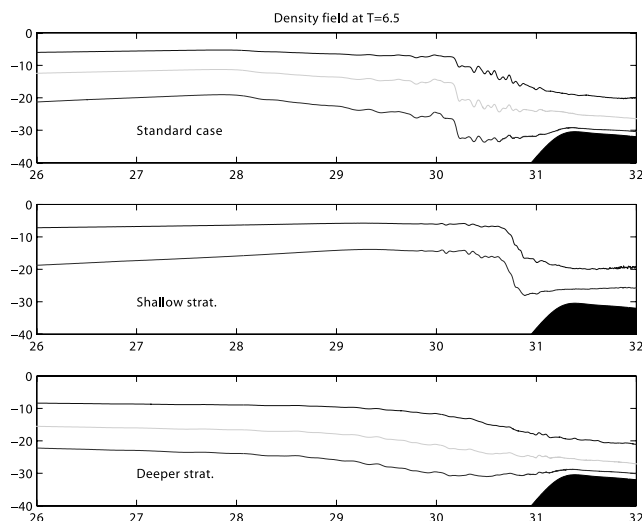

Figure 8. Density field 6.5 hours after beginning of ebb tide, with (top) mean stratification, (middle) shallower and (bottom) deeper pycnocline. Isolines are as in Figure 5.

downstream during spring tide and with shallow stratification. During neap tide, it is released earlier, and similarly with deeper stratification. However, during neap tide, the disturbance begins to evolve into an undular bore as soon as it leaves the crest, while, when a deeper pycnocline is present, it does not evolve into an undular bore until further away from the crest (see discussion below). These results refute the "lee wave" theory advanced by Haury and coworkers [*Haury et al.*, 1979, 1983]. Rather, the effect of the ebbing flow over the bank is to create a pool of light water, which is subsequently released. Thus a lock-exchange scenario seems to be more appropriate model for the generation mechanism.

5.2. From Depression to Undular Bore

[30] As the tide slacks, the depression begins to move westward (Figures 7 and 8). In the standard case, the western side of the depression moves over and away from the crest as a rarefaction wave (leading edge moving faster than trailing edge, see Figure 7), before developing into an undular bore at $t = 7$. The amplitude of the leading wave is about 30 m (Figure 9). During neap tide conditions, we observe a similar development. However, the depression is released earlier and the leading edge has already evolved into an undular bore at slack tide. The amplitude of the leading wave is smaller. The situation is quite the opposite during spring tide. The depression is still east of the crest at slack tide, while at $t = 7$, it is moving west of the bank, undergoing the initial rarefaction process. As in the previous cases, the disturbance develops into an undular bore of somewhat larger amplitude.

[31] Overall, the main impact of variations in the forcing strength at this stage is on the release time, related to how further downstream the depression is advected during ebb, as well as to the strength of the ensuing undular bore. This result agrees with the observed increase of arrival time with amplitude of the forcing observed during the MBIWE98 (Figure 10b).
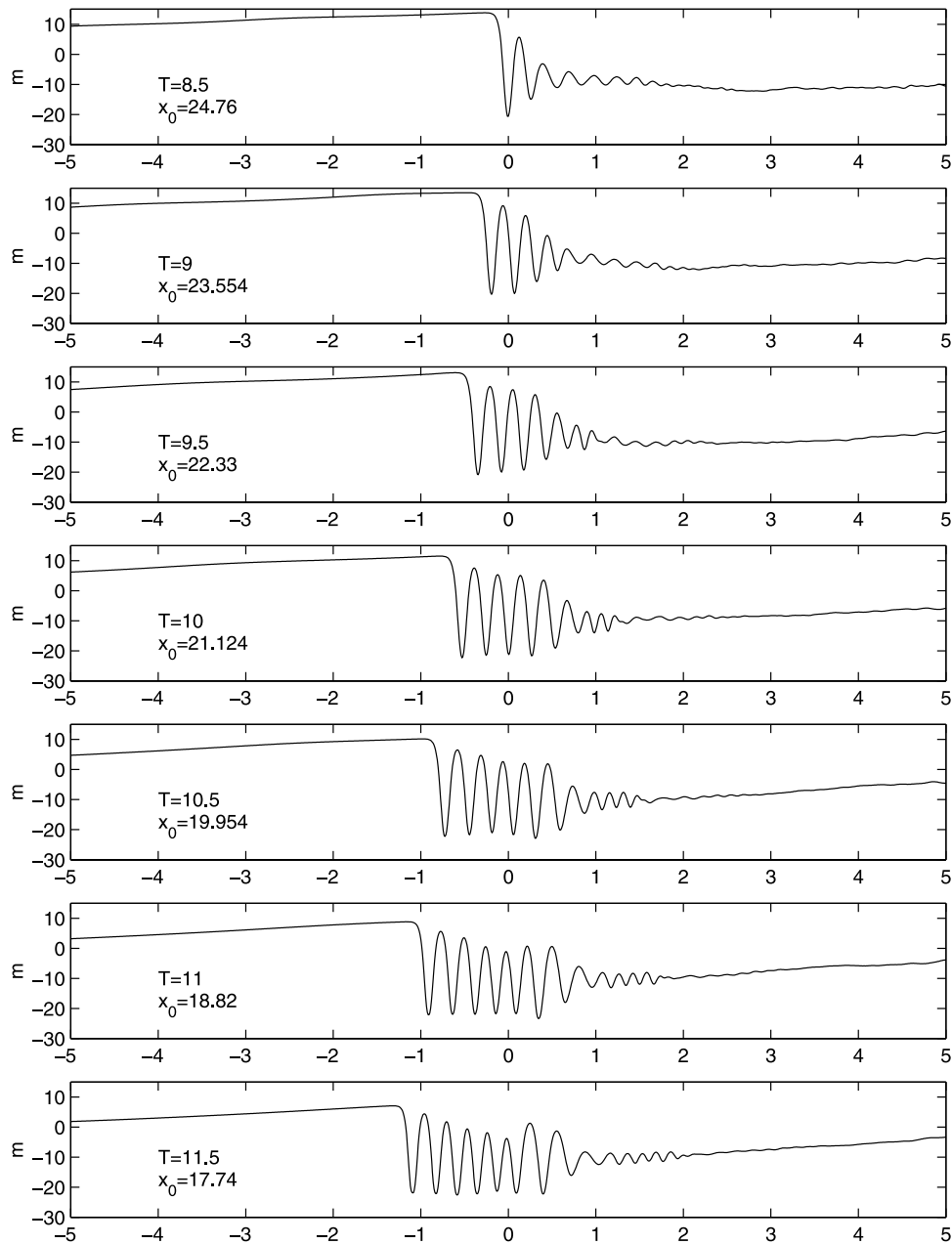
Figure 9. Displacement of the pycnocline in Stellwagen Basin during the passage of the undular bore under standard conditions. The disturbance is plotted in a frame of reference moving with the linear wave speed (corrected for the barotropic tide). Here x_0 is the position of the origin in the coordinates employed in Figure 2. Horizontal distances are expressed in kilometers. The time is relative to the onset of ebb.

[32] Differences in stratification have more substantial effects during the early stage of propagation. With shallower stratification (that is, smaller linear phase speed), the western side of the depression quickly evolves from a rarefaction wave into an undular bore. A deeper stratification has an opposite effect. The leading edge of the rarefaction wave moves rapidly away, and the undular bore emerges more slowly. This prediction is corroborated by the analysis of field data (Figure 11).
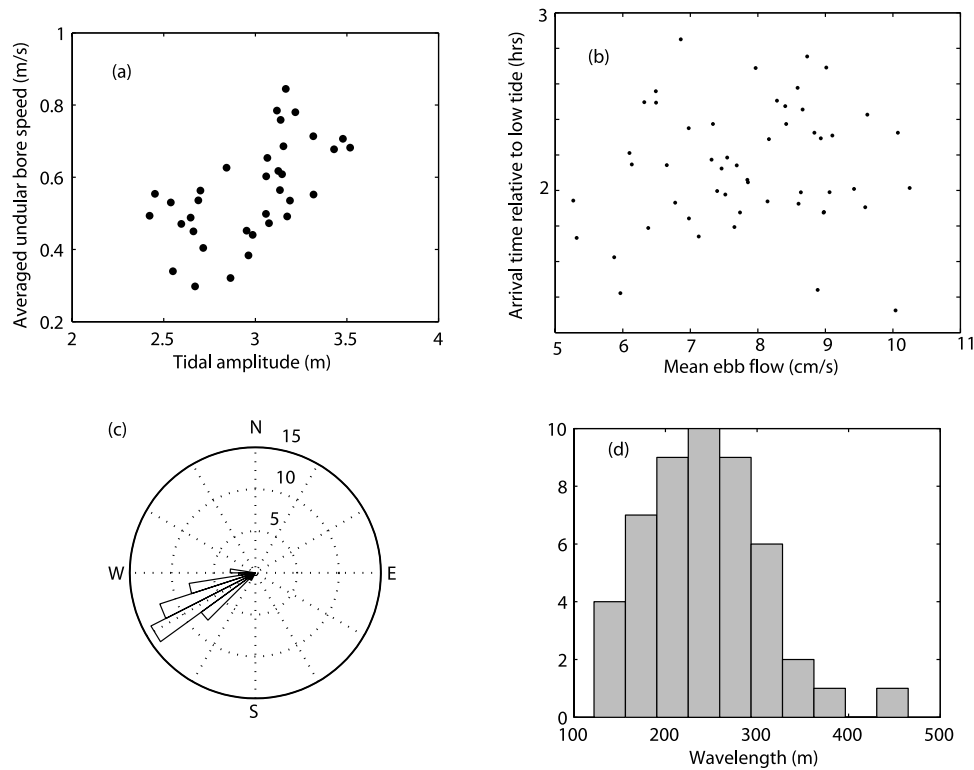
5.3. Propagation in the Basin

[33] Away from the generation region, the depression evolves as an undular bore, with a mode one structure,

and it is convenient to discuss the propagation in terms of normal modes.

5.3.1. Standard Conditions

[34] During the generation phase, the blocking action of the sill raises the pycnocline ahead of the depression. As the wave leaves the generation area, the pycnocline is first slowly raised, of an amount that decreases as the wave propagates: from as much as 15 m when the wave is just west of the sill, to about 5 m in the middle of Stellwagen Basin (Figure 9). The passage of the undular bore leaves the pycnocline about 10 m below its equilibrium position, slowly rebounding during the rest of the tidal cycle. The

Figure 10. Propagation characteristics during MBIWE98. (a) Undular bore speed versus tidal amplitude at B. (b) Scatterplot of arrival time of the leading edge of NLIWs packets (relative to low tide in the basin) versus mean intensity of barotropic flow in the basin (a proxy for the intensity of the tide over the bank) at A. (c) Direction of propagation at B. (d) Distribution of wavelength at B. For mooring location, see Figure 1.

amplitude of the leading wave (measured taking the difference between the upward displacement just ahead of the bore and the downward displacement immediately after) is about 35 m when the wave reaches the basin, and decreases to about 25 m as the wave approaches the western rise of the basin. The reduction in amplitude is entirely due to the reduction in the upward displacement immediately after the passage of the wave. The undular bore propagates with an average speed of 0.64 m/s (corrected for the barotropic shift), to be compared with the speed of linear waves, which is 0.55 m/s in the basin. This value agrees well with the measured speed in the basin, which is clustered around 0.60 m/s (Figure 10). The wavelength of the high-frequency oscillations is within the bounds observed in the area (Figure 10d), and in fact appears to be quite insensitive to the strength of the forcing and the depth of the thermocline.

5.3.2. Spring Tide

[35] During spring tide, the evolution is qualitatively similar to the standard case (Figure 12). The upward displacement upstream of the disturbance is somewhat larger, ranging from 15 m on the eastern side of the basin to 5 m on the western side. The downward displacement of the pycnocline after the passage of the undular bore is also larger, about 15 m, and the amplitude of the leading wave is larger as well, almost 40 m in the middle of the basin. The trough of the solitary waves are flattened out, which is to be expected for strongly nonlinear waves
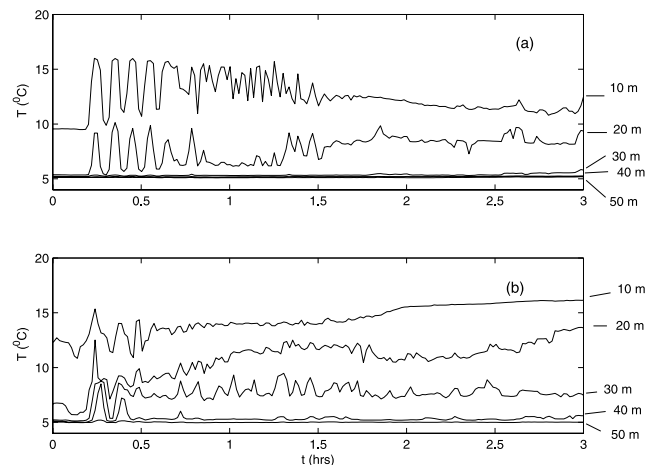
Figure 11. Temperature records at mooring A (Figure 1) during the passage of two different trains of NLIWS. In both cases, time is measured in hours relative to the arrival of the first wave. The two events are 1 week apart. The depth of the thermistors is indicated on the right side. (a) The pycnocline is shallow (about 5 m below surface). (b) The pycnocline has deepened to about 12 m.
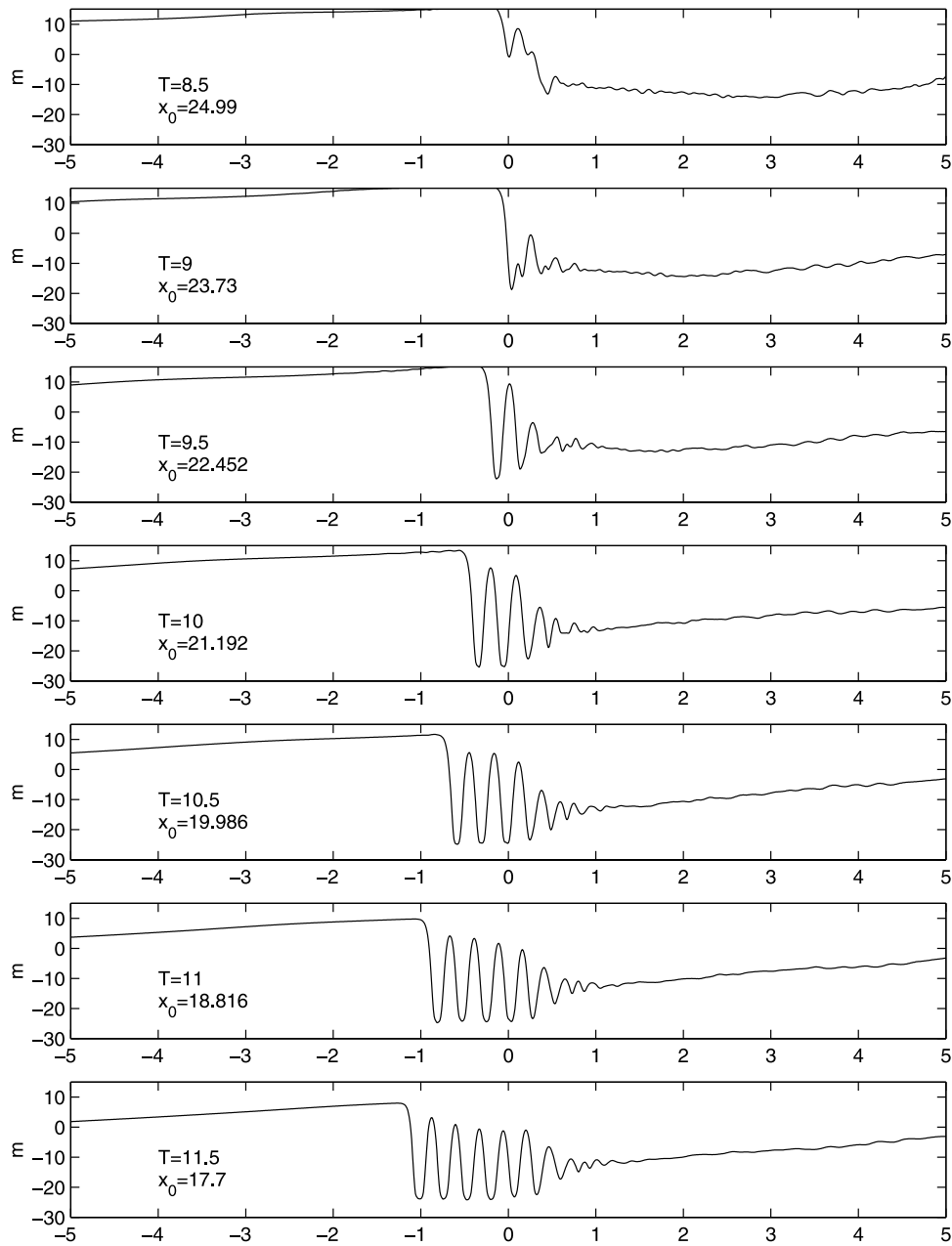
Figure 12. Same as Figure 9, but during spring tide.

[*Stanton and Ostrovsky*, 1998]. Despite the larger overall amplitude, the speed of propagation is slightly smaller, 0.61 m/s, signaling a departure from the weakly nonlinear regime.
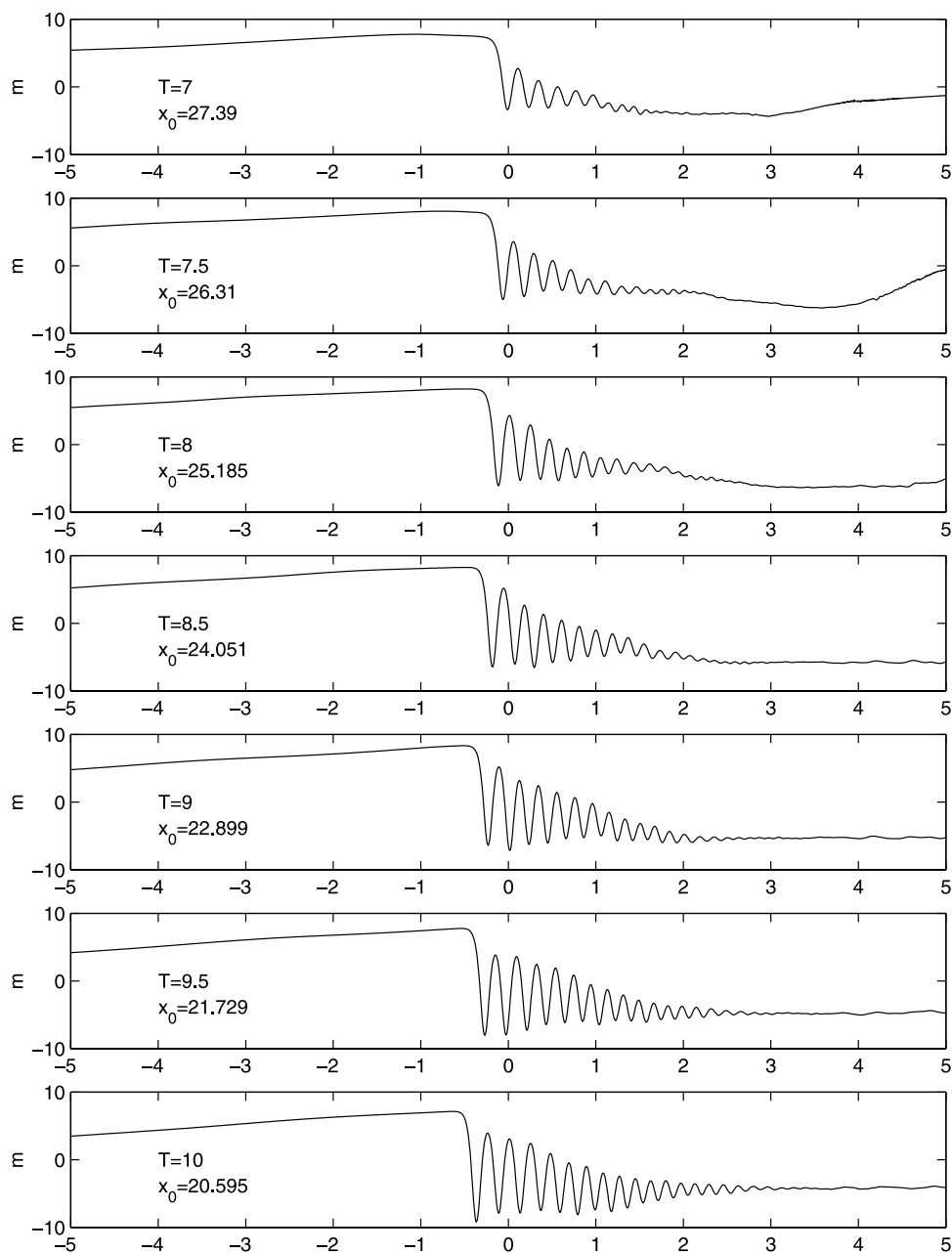
5.3.3. Neap Tide

[36] During neap tide, the wave generated has overall a smaller amplitude. The maximum upward displacement is slightly smaller than 10 m, while the passage of the undular bore leaves the pycnocline only 5 m below the equilibrium level (Figure 13). The nature of the undular train is also different. During spring and normal conditions, the train evolves toward a state characterized by a number of large oscillations not necessarily rank ordered (e.g., $t = 11.5$ in

Figure 9) which end rather abruptly to leave space to small amplitude oscillations of the depressed pycnocline. In the present case, the amplitude of the oscillations continuously decreases, as we move from the front to the back, and the total number is larger. Also, the packet moves at a mean speed only slightly larger than the linear wave speed.

5.3.4. Shallower Pycnocline

[37] The propagation on a shallower pycnocline follows the same pattern described above (see Figure 14). Since in this case the linear wave speed is lower, the wave is advected further downstream during the generation process, hence it leaves the crest later. The upstream upward displacement remains fairly constant during the propagation

Figure 13. Same as Figure 9, but during neap tide.

(10 m). During the early stage, the overall pycnocline displacement initially increases from 10 to 15 m, up to $t = 8.5$, after which the displacement decreases to about 10 m again, as the undular bore progresses, while the amplitude of the leading wave remains fairly constant, about 30 m. Up to $t = 8.5$, the packet has a well defined beginning, while at later times, the amplitude of the oscillations decreases smoothly, and, unlike the other cases considered, both the downward and upward displacement of the waves decreases. Overall, the NLIWs predicted by the model reproduce the features observed in the field. Quantitatively, the propagation speed of the undular bore follows the pattern observed in the field, as well as the timing with

respect to the barotropic tide, though the field data have a larger scatter.

5.4. Energetics

[38] The energy flux associated with the wave packets have been discussed in detail by *Scotti et al.* [2006] to which we refer the reader for details. The model predicts fluxes associated to the high-frequency component of the waves ranging from 1500 W m^{-1} for standard conditions to 700 W m^{-1} with a shallow stratification, within the range of fluxes observed in the field. There is a correlation in the field data between the energy flux associated to the nonlinear waves and the depth of the pycnocline (Figure 15) such that a deeper pycnocline is associated to a stronger energy
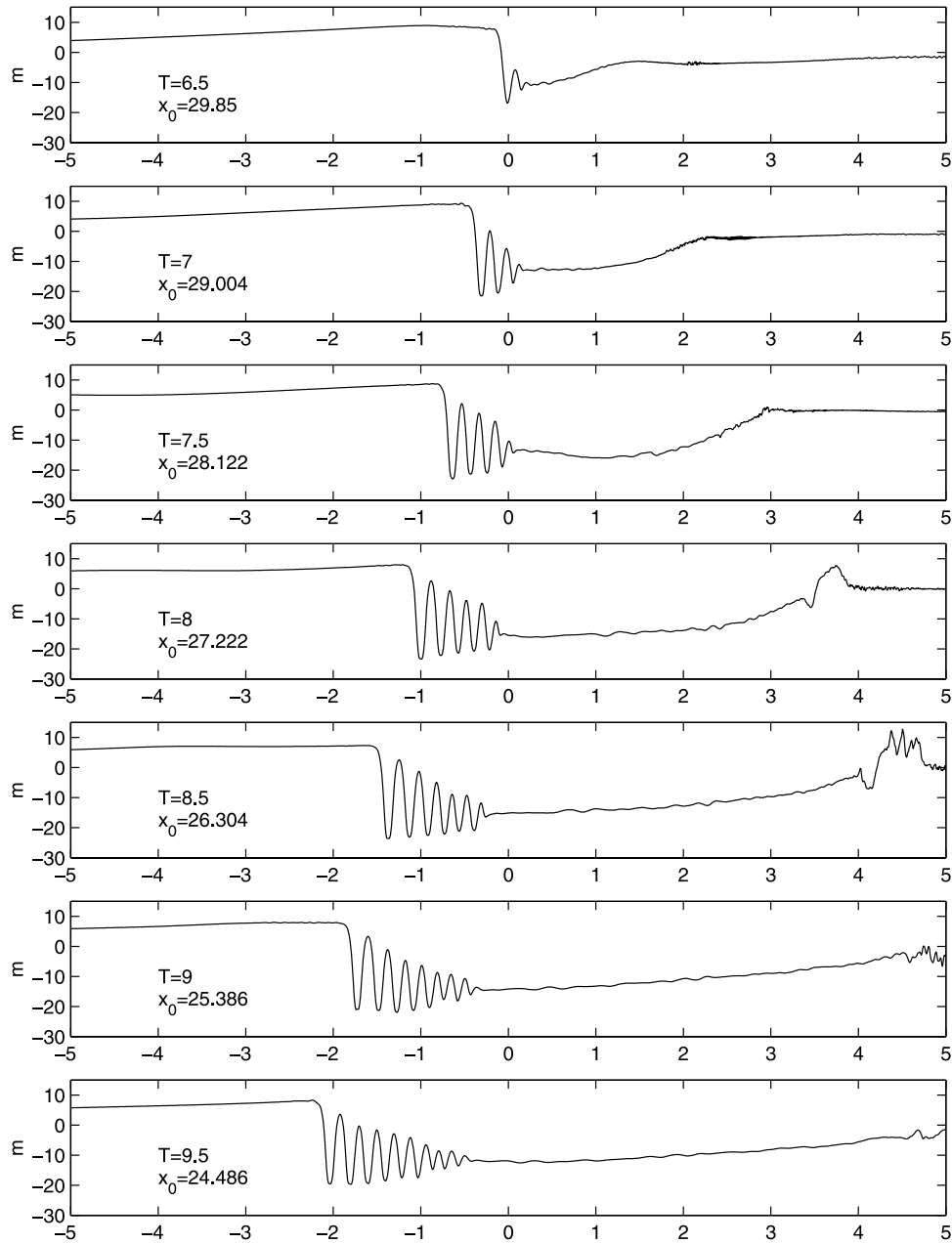
Figure 14. Same as Figure 9, but with a shallower pycnocline.

flux. A similar correlation exist in the modeled data. This correlation may play a role in controlling the seasonal development of the pycnocline in the area. As the thermocline deepens, the NLIW-induced diapycnal mixing increases to the point where the heat flux across the pycnocline balances the heat input from the surface.

6. Discussion

### 6.1. Nonlinearity Versus Dispersion During Generation and Propagation

[39] To asses the importance of nonlinearity over dispersion, we run the model in the long-wave limit, as explained earlier, as well as a linearized version of the dispersive

model, in which the advective terms $J(\psi, \cdot)$ was replaced by $J(\overline{\psi}, \cdot)$, where $\overline{\psi}$ is the barotropic component of the stream function, that is the solution of

$$\nabla^2 \overline{\psi} = 0, \tag{11}$$

subject to the same boundary conditions. In both cases, we considered standard tidal forcing and stratification.

[40] During the generation phase, the long-wave model differs from the full model in two details: (1) small-scale instabilities are absent (as they are filtered out by the cutoff filter) and (2) the western edge of the depression is slightly broader. The linearized model is only qualitatively similar. The major quantitative difference is that the upstream side
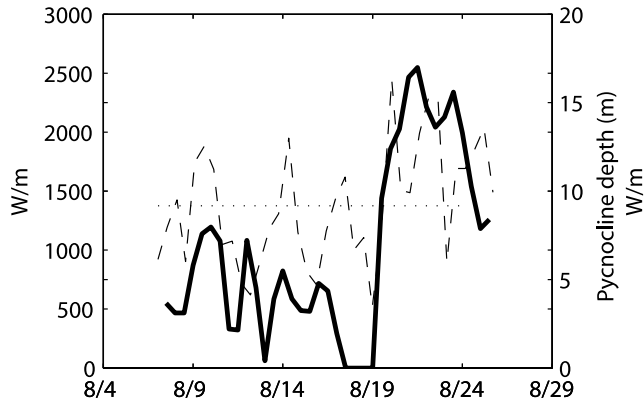
Figure 15. Mean energy fluxes (dashed line) and depth of pycnocline (solid line) measured at B during MBIWE98. The fluxes are calculated following *Scotti et al.* [2006] and averaged over the extent of the NLIWs packets.

of the depression over the bank is advected farther downstream (Figure 16).

[41] During the propagation in Stellwagen Basin, the effects of dispersion becomes of course important when the nonlinear term ''activates'' smaller wavenumbers through the steepening of the wave. It is, however, interesting to note that the long-wave model predicts a bore of equal amplitude and speed as the full model. The linearized model, on the other hand, simply assumes that the waveform generated on top of the bank moves westward with some distortion due to dispersion. Thus we see that at least during generation nonlinearity remains the dominant force in shaping the flow. We now turn to simplified models to discuss the physical meaning of these results.

6.2. Generation

[42] *Hibiya* [1988] was the first to develop a conceptual model for the generation of internal waves over Stellwagen Bank. He convincingly argued that the generation is essentially a time-dependent phenomena, as opposed to the evolution of a quasisteady system of lee waves. He proposed a mechanism by which, during the supercritical phase of the ebb tide, upstream-moving infinitesimal waves (i.e., waves that in the absence of a barotropic flow would flow westward) are generated over the bank and carried downstream (eastward), until they reach the point where their linear phase speed matches the barotropic flow. There they are amplified until the tide slacks, and the resulting large amplitude internal wave is released.

[43] In mathematical terms, Hibiya's model is based on the assumption that the Riemann invariants emanating from the bank propagate along characteristics given by

$$\frac{dx^{\pm}}{dt} = c_{\pm} \simeq \frac{Q}{D-h} \pm c_0\left(x^{\pm}\right), \quad (12)$$

where c_0 is the linear wave speed of the corresponding mode and Q the barotropic transport. In other words, his model neglects the changes in the speed of propagation induced by the growing disturbance. The fact that the linearized model captures qualitatively the features observed

over the bank during the generation process supports Hibiya's theory. The nonlinear dependence of c upon the flow conditions must be responsible for the difference in location of the upstream side of the depression, since dispersion does not seem to play a major role.

[44] As the tide slacks, the depression begins to move westward. If the bottom had constant depth, the natural tendency would be for the leading edge to steepen. However, the steepening is delayed by the change in linear speed and baroclinic advection caused by the dropping bottom. If we recast the two-layer model (equation (8)) in characteristic form, the speed along the upstream-directed characteristics is given by [*Baines*, 1995]

$$c_- = \frac{Q}{D-h} + \frac{v(d_2 - d_1)}{D-h} - \sqrt{\left(g'(x) - \frac{v^2}{D-h}\right)\frac{d_2 d_1}{D-h}}. \quad (13)$$

The interplay of baroclinic advection (second term) and buoyancy wave speed controls the evolution of the characteristics, and in turn the slope of a disturbance (see Appendix B for a brief review of solving hyperbolic systems using characteristics). For a westward moving disturbance, a decrease in c_- toward the west (i.e., $dc_-/dx < 0$) will cause the disturbance to steepen, since the through moves faster than the leading edge. In deep water, and with $d_2 < d_1$, a westward moving depression will thus have its western slope steepening ($c_{nl} = \sqrt{(g' - v^2/D)d_1 d_2/D}$ increases with d_2 as long as $d_2 < D/2$, and the other terms are usually negligible). In shallow water (relative to the amplitude of the disturbance), baroclinic advection and smaller values of d_1 can change the picture, and a wave of depression can actually be smoothed out. The former mechanism is clearly at play in the middle of Stellwagen Basin, while the latter plays an important role during the late stage of generation, as well as during shoaling. In Figure 17 we show the displacement of the pycnocline and the speed of the westward characteristics at $t = 4$, 5.5, 6 and 6.5 (the displacement and baroclinic velocity where calculated from the output of the fully nonlinear and dispersive model). At $t = 4$, the flow is still supercritical over the crest, and $dc_-/dx < 0$ across the jump. As the tide slacks and the jump begins to
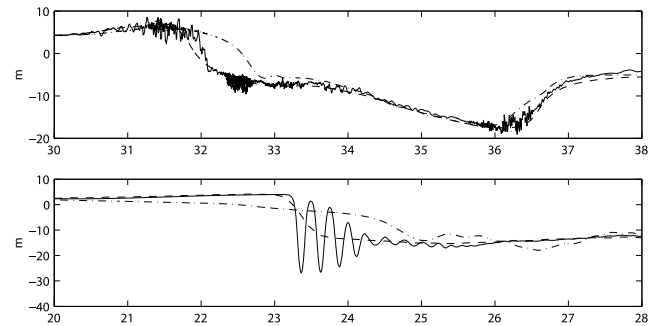
Figure 16. Displacement of the 20-m isoline predicted by the full model (solid line), long-wave model (dashed line), and linearized model (dash-dotted line), (top) at $t = 5$, when the depression is over the bank, and (bottom) at $t = 9$, when the undular bore is in the middle of the basin. Standard conditions apply to all cases.
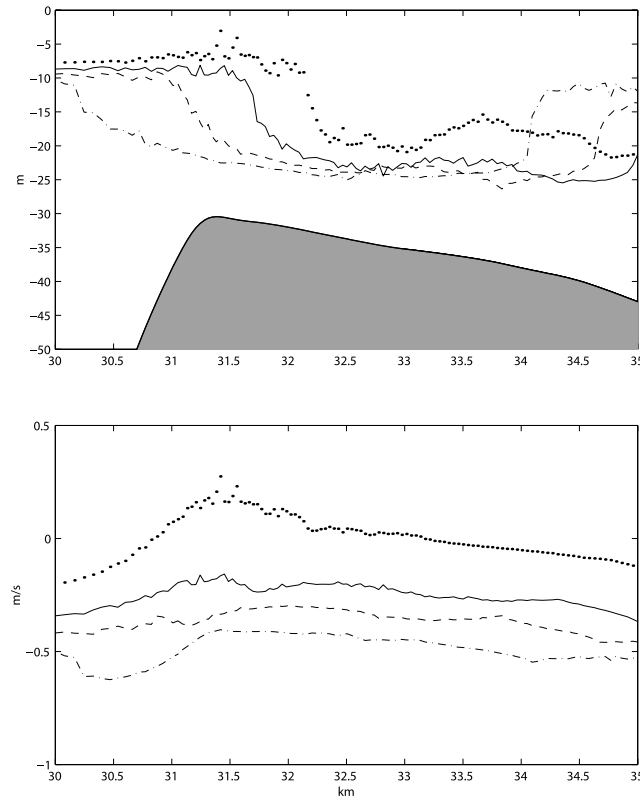
Figure 17. (top) Displacement of the pycnocline over Stellwagen Bank at four different times during the generation phase and (bottom) speed of the westward going characteristics. Symbols are as follows: dotted line, $t = 4$; solid line, $t = 5.5$; dashed line, $t = 6$; dash-dotted line, $t = 6.5$. Displacement and baroclinic velocity were obtained from the full model.

move upstream, dc_-/dx becomes positive over a larger and larger portion of the jump, whose slope decreases. At $t = 6.5$, the leading edge of the depression has reached the basin, and we see that there is still a small, but significant, portion of the jump where $dc_-/dx < 0$. This is the seed that will evolve into the undular bore over the basin. This mechanism explains the different behavior observed with different stratification. The difference in linear wave speed for a shallower pycnocline between the top of the crest and the midbasin is smaller, thus the effect of the dropping bottom is lessened. Vice versa, a deeper pycnocline heightens the influence of the dropping bottom. Also, the flow is supercritical for a shorter period. As a result, the slope of the jump after emerging from the generation area is much reduced, and the time required for nonlinearity to rebuild it while it propagates in the middle of the basin is longer.

6.3. Propagation

[45] Table 3 reports the significant parameters of the wave packets computed from the solution of the full model. The first thing to notice is that these waves have very large amplitudes and relatively short wavelengths, thus we expect that a description in terms of solutions of the KdV equation will be qualitative at best. In all cases considered, the passage of the packet leaves the pycnocline depressed.

The packet generated during mean and spring tide conditions share similar characteristics as they leave Stellwagen Basin: a number of large oscillations not necessarily rank ordered, followed by a number of smaller amplitude waves, with a sharp transition between the two, especially in the standard case (see, e.g., $t = 11.5$ in Figure 9). The speed of propagation is also similar. During neap tide, the oscillations have a smaller amplitude, the packet is longer and the amplitude decreases continuously as one moves from the front to the back. The evolution of the packets in the shallower pycnocline case follows an intermediate path. During the earlier stage of propagation, the packet has a well defined end, but gradually the transition becomes smoother, a process that continues over the slope. The evolution of the packets, especially during neap tide and with shallower pycnocline is reminiscent of a little known solution to the KdV equation, first introduced by *Gurevich and Pitaevskii* [1973a, 1973b] to study shocks in collisionless plasmas, and used in this context by *Grimshaw and Smyth* [1986] and *Apel* [2003]. If at $t = 0$, we have a single shock of amplitude $2\eta_0$, located at $x = 0$ for simplicity, the traveling solution at a later time t will be found as follows. Define a parameter τ as

$$\tau = \frac{x - c_0 t}{\alpha \eta_0 c_0 t}. \tag{14}$$

At time t, the packet is confined over the strip defined by $-1 \leq \tau \leq 2/3$. Also, for each $\tau \in [-1, 2/3]$, solve the equation in $s \in [0, 1]$ implicitly defined by

$$\tau = \frac{1}{3}\left(1 + s^2\right) - \frac{2}{3}\frac{s^2(1 - s^2)K(m)}{E(m) - (1 - s^2)K(m)}, \tag{15}$$

with $K(m)$ and $E(m)$ as the complete elliptic integrals of first and second kind, respectively [*Abramowitz and Stegun*, 1964], whose argument is $m = s^2$. Then the traveling wave can be written as

$$\eta(x, t) = \eta_0 \left\{ 2\mathrm{dn}_s^2\left[\frac{k_0\alpha\eta_0 c_0 t}{2}\left(\tau - \frac{1 + s^2(\tau)}{3}\right)\right] - \left(1 - s^2(\tau)\right) \right\}, \tag{16}$$

where $k_0/2 = \sqrt{\alpha\eta_0/6\gamma}$, and dn_s is an oscillatory Jacobi elliptic integral, called sometimes the dnoidal solution, in analogy to the well-known cnoidal solution.

Table 3. Basic Parameters of the Wave Packets Observed Propagating in the Middle of the Basin[a]

	Speed, m/s	Wavelength, m	Maximum Amplitude, m	Final displacement, m
Standard	0.65	200	29	10
Spring tide	0.64	250	32	12
Neap tide	0.59	200	16	4.2
Shallow pycnocline	0.56	230	28.8	10

[a]Speed, wavelength (measured as the distance between the first and second trough), amplitude, and final downward displacement are calculated from the packets at the western end of the basin, just before the beginning of the shoaling area.
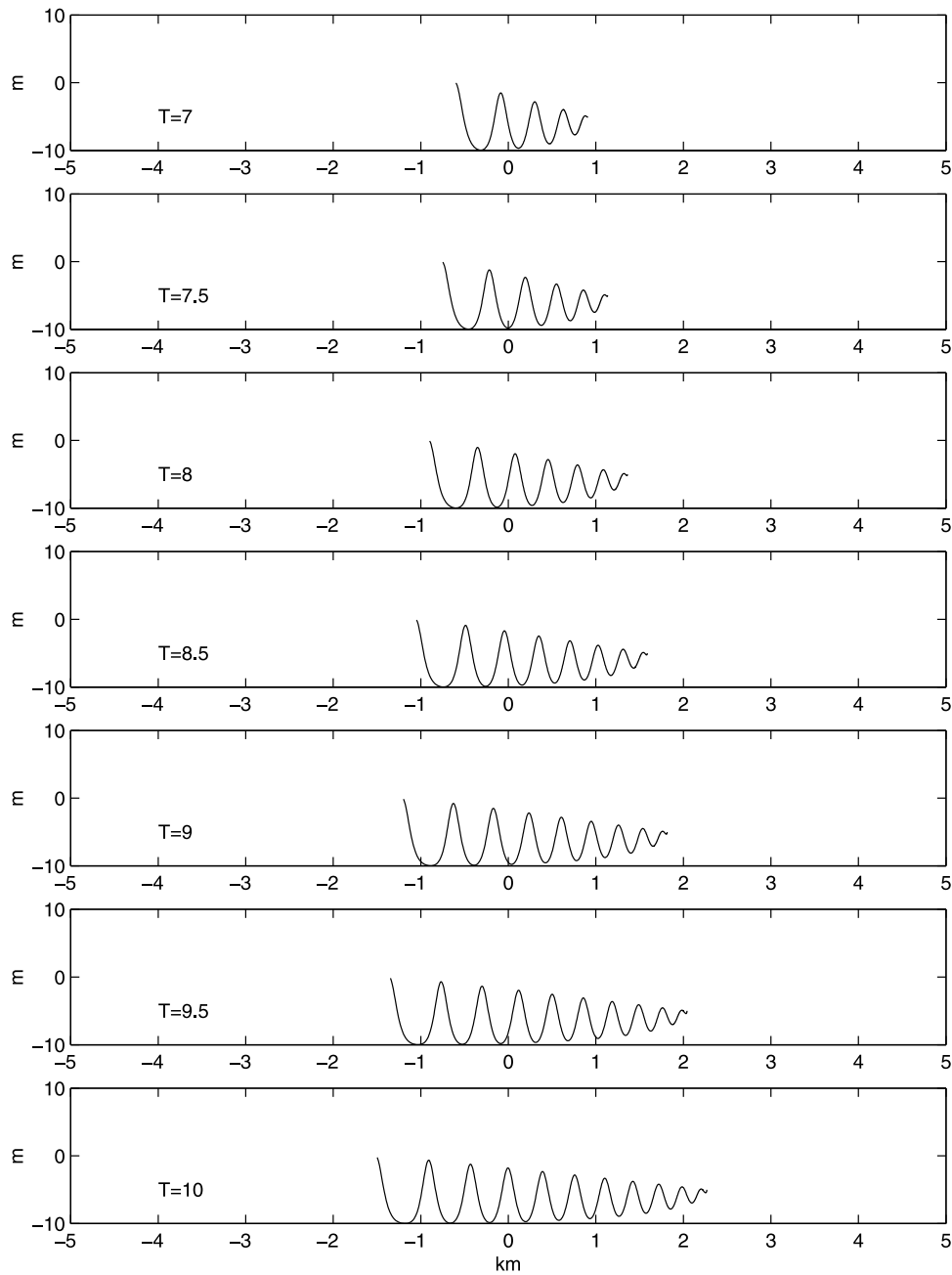
Figure 18. Evolution of the dnoidal solution to the KdV equation over the same period considered in Figure 13. The parameters are $k_0/2 = .011$ m^{-1} and $\eta_0 = 5$ m.

[46] Unlike the classical soliton pulse solution and the periodic cnoidal waves, the dnoidal solution does not represent a traveling wave, but rather a similarity solution which at $t = 0$ takes the form of a shock which disintegrates over time into a series of oscillations of decreasing amplitude and wavelength. The size of the packet increases at a rate given by $\alpha\eta_0 c_0$, and the wavelength increases going from the front to the back, where it reaches the asymptotic value of $2\pi/k_0$. In Figure 18, we show the dnoidal solution for a packet propagating over the observed stratification with an amplitude chosen to match the one observed during neap tide (5 m). The rate of spread and nonlinear wavenumber have been computed using the values reported in Table A1. Qualitatively, the agreement is good. Quantita-

tively, the rate of spread of the packet roughly matches the observed one, while the wavelength of the oscillations is overestimated. Also, the leading edge propagates faster relative to the centroid of the packet in the KdV case, as shown in Table 4. The large discrepancy between observed and computed propagation speed is expected, and mirrors similar observations in different areas, for example, the Sulu Sea [*Apel et al.*, 1985].

[47] The agreement, which could in principle be improved were we to regard k_0 and $\alpha\eta_0$ as free parameters to be computed from the rate of spread and the observed wavelength on the lee side of the undular bore, is in large part due to the fact that the amplitude of the undular bore during neap tide is relatively small.

Table 4. Speed of Propagation and Wavelength of Single Pulse Solitary Solutions of the KdV Equation Using the Amplitudes From Table 3 and the Parameters From Table A1

	η_0, m	V, m/s	Δ, m
Standard	29	0.79	213
Spring tide	32	0.82	203
Neap tide	16	0.68	287
Shallow pycnocline	28.8	0.64	152

[48] During standard and spring tide conditions, it is harder to coax the dnoidal solution into reproducing the observed behavior. During standard conditions, the packet has dnoidal characteristics during the early stage of development, up to $t = 8.5$ (Figure 9). However, the packet assumes a more cnoidal look thereafter. A similar observation holds for the packet evolving during spring tide. Quite the opposite seems to happen when we consider a shallower stratification. Here the packet has a cnoidal connotation at the beginning, but later transitions toward a dnoidal state, which is maintained thereafter. It is possible that the inclusion of a cubic term in the KdV equation [*Helfrich and Melville*, 2006] may improve the accuracy of the model.

7. Summary

[49] In this paper we have used a fully nonlinear, non-hydrostatic model to study the generation and propagation of large internal waves in Mass Bay under different environmental conditions. The study was motivated by the need to provide a theoretical framework for the interpretation of data collected in the region during the 1998 Massachusetts Bay Internal Wave Experiment. According to our model, the waves observed in Mass Bay begin their lives as a depression in the pycnocline developing over Stellwagen Bank, to the east of the crest, during ebb tide, in accordance with the observations of *Chereskin* [1983] and the modeling effort of *Hibiya* [1988]. As the tide slacks, the depression begins to move westward. During the generation phase, nonlinearity dominates, so much so that a fully nonlinear but longwave (hydrostatic) model gives essentially the same results at large scales. The normal tendency of the western edge of the depression as it moves westward would be to steepen, because of nonlinear effects. However, the relatively rapid change in bottom topography immediately to the west of the bank acts against nonlinearity, so that the leading edge of the depression tends to become less steep as it leaves the crest, until the smoothing effect ceases when it reaches the eastern edge of Stellwagen Basin. The effect is more pronounced the larger the difference in linear wave speed between the crest and the basin. The wave bounding to the east the original depression becomes trapped just west of the bank, as the ebbing flow becomes supercritical again, so that what was a $O(5 \text{ km})$ wide depression over the bank eventually becomes a bore, and after the slope of the leading edge becomes steep enough that dispersion is significant, an undular bore. The transition from bore to undular bore depends on how soon the smoothing effect of the changes in topography wanes, which in turn depends of the details of the stratification, as well as the amplitude of the original disturbance. Thus, at a fixed location, the number of high frequency waves making up the wave packet depends on the details of the upstream stratification. The basic dynamics up to the point where the bore becomes undular can be explained in terms of a simple two-layer hydrostatic model. This picture is consistent with the data from MBIWE98 where it was observed that waves generated during spring tide took longer to arrive at mooring A than the ones generated during neap tide, even though the latter were smaller.

[50] In the middle of the basin, dispersion cannot be ignored. We have shown that a similarity solution of the KdV equation qualitatively explains the observed evolution, especially when the amplitude of the oscillations is small and the KdV equation is formally valid. This seems to be the case only for the packets generated during neap tide and the late stage of the undular bore propagating on the shallow pycnocline. For large-amplitude packets the dynamics is more complex, as the undular bores switch from a dnoidal to a cnoidal-like behavior.

[51] The baroclinic energy flux predicted by our model agrees well with the observed values. We find that the flux increases when the thermocline deepens. On average, the bank radiates 60 MW of baroclinic energy, of which 60% is directed toward shore. This value is negligible compared with the barotropic tidal energy dissipated within the Gulf of Maine, which is estimated to be about 50 GW [*Greenberg*, 1979]. However, this energy is "immediately" available for mixing in the interior of the basin.

[52] As our main focus has been on the development of large internal waves in Mass Bay, we have not discussed waves propagating to the east of the sill. The asymmetry of the bank is reflected in the asymmetry of the response of the pycnocline to the forcing. In agreement with the observation of *Chereskin* [1983] and R. Geyer and E. Terray (personal communication, 2006), our model predicts a much narrower depression forming on the western side of the bank during flood phase (about 1 km wide). When the tide turns, the eastern side propagates to the east as an undular bore of smaller amplitude relative to its western counterpart. Owing to the gentler slope of the eastern side, no initial smoothing was observed.

[53] To summarize, the large internal waves observed in Mass Bay begin their life as a nonlinear process where dispersion plays a marginal role and evolve in the middle of the bay under the combined effects of nonlinearity and dispersion.

[54] Several issues remain open. For example, we do not know to what extent the response of the flow over the bank to the time varying forcing can be considered adiabatic, and an extended, forced KdV equation can be used to study it [see, e.g., *Grimshaw and Smyth*, 1986]. Our model captures well the qualitative features of nonlinear waves in the area and quantitatively it reproduces well the range of bulk properties, such as energy fluxes, overall displacement of the pycnocline and speed of propagation. However, the model fails to reproduce the large variability observed in the detailed properties of NLIWs packets. For example, at mooring A, the number of NLIWs found at the leading edge of the undular bore ranged from as low as 1 to over 30. Mean depth of the pycnocline and strength of the forcing along do not explain the variability, since the number of NLIWs was found to be highly variable even during periods of relatively constant pycnocline depth and forcing, with

large variations from one cycle to the next. It is possible that three-dimensional effects may play an important role, which cannot be investigated with the present model. We also need to consider that the underlying dynamics is nonlinear and quite likely dissipative. From the theory of dynamical systems, we know that the two conditions lead quite naturally to chaotic systems. Lacking measurements over the bank itself, we cannot settle the question.

[55] Finally, the observation that the properties of generation and, in an appropriate sense, propagation can be captured by a fully nonlinear but hydrostatic model, provided dissipation is accounted, raises the possibility of introducing parameterizations that can be used to account for NLIWs in hydrostatic models, at least when the nonlinear process feeding energy into NLIWIs (in the case considered here, an internal bore) can be represented on a coarse (i.e., hydrostatic) grid. In such a configuration, the principal nonhydrostatic effect consists in removing energy from the bore, energy which is radiated away as nonlinear waves. In the hydrostatic (coarse-grained) simulations performed here, the spectral filter removes energy from the high-wavenumber end of the spectrum, while maintaining unaltered the shape of the spectrum of the resolved scales. The latter is important to ensure that the nonlinear transfer of energy from low to high resolved wavenumbers is not affected. Whether this energy is radiated as NLIWs or locally dissipated appears to have little effect on the large-scale properties of the bore (amplitude, speed of propagation, ...). Thus the fundamental elements for parameterizing NLIWIs seem to be (1) not disturbing the nonlinear energy flux to small scales and (2) extracting energy at the proper rate, controlled by the nonlinear energy transfer rate. As it is often the case when parameterizing subgrid-scale effects, the problem cannot be easily separated from the numerical discretization employed. In particular, the existence of numerical dispersion (virtually absent in the spectral discretization employed here) implies that some energy will be radiated as high-frequency "numerical" NLIWs (O. Fringer, personal communication, 2007), and thus the dissipation will have to be reduced accordingly. In this respect, it is likely that the best course will be to establish basic "Shock" conditions (see Appendix B), to be adapted to the specific model considered. The dnoidal solution (or the equivalent for the eKdV case) can provide the starting point for such an analysis.

Appendix A: Derivation of Parameters Used in Simplified Models

[56] To compute the parameters entering the KdV equation we follow *Liu and Benney* [1981], who derived the coefficients for a continuously stratified fluid in terms of the mode 1 eigenfunction ϕ as follows

$$\alpha = \frac{3}{2Q} \int_h^D (d\phi/dz)^3 dz, \quad \beta = \frac{1}{2Q} \int_h^D (\phi)^2 dz, \quad (A1)$$

$$Q = \int_h^D (d\phi/dz)^2 dz, \quad (A2)$$

and c_0 and ϕ are the gravest solutions of the eigenproblem

$$\frac{d^2\phi}{dz^2} + \frac{N^2(z)}{c_0^2}\phi = 0, \quad (A3)$$

with boundary conditions $\phi(h) = \phi(D) = 0$ and $\max(\phi) = 1$. Note that the flow considered in our simulation did not have any background shear. We have chosen the density profile and bottom depth at $x = 23.5$ km as representative of the basin.

[57] For the two-layer case, the relevant parameters are the depth of the overlaying layer d_{20} and the reduced gravity $g' = g\Delta\rho/\rho$. The depth of the upper layer can be assumed to coincide with the maximum in the Brünt-Väisäla frequency (that is, the depth of the pycnocline). The reduced gravity was computed locally by calculating the difference between the mean density above and below the pycnocline. In this way, the linear long-wave speed $\sqrt{g'(x)d_{10}d_{20}/(d_{10} + d_{20})}$ is roughly equivalent to c_0 introduced above. Table A1 reports the value of the parameters used for the KdV model.

[58] The amplitude η that appears in the KdV model is related to the baroclinic component of the stream function ψ_b by

$$\eta = \frac{b1}{c_0}, \quad (A4)$$

$$\psi_{b1}(x,t) = \int_h^D \psi(x,z,t)\phi(z)N^2(z)dz / \int_h^D \phi^2(z)N^2(z)dz, \quad (A5)$$

which follows from the derivation of the model. For the two-layer model, η is defined as the displacement of the pycnocline depth, while the baroclinic velocity v is given by

$$v = -\frac{b1}{D-h}. \quad (A6)$$

Appendix B: Characteristics and Shock Formation

[59] The solution of a system of N hyperbolic conservation equations such as equation (8) can be obtained by the method of characteristics [*Courant and Hilbert*, 1989]. From the initial condition, N appropriate quantities (the Riemann invariants) are formed, that remain constant (if no source terms are present in the conservation equations) along trajectories in space-time given by

$$\frac{d\mathbf{x}}{dt} = c_i(\mathbf{x}), \quad i = 1, \ldots, N, \quad (B1)$$

Table A1. KdV Parameters Associated With the Stratifications Considered

	c_0, m/s	α, m^{-1}	β, m^2
Standard	0.55	−0.0458	316
Shallow	0.38	−0.0732	255
Deep	0.73	−0.0288	364
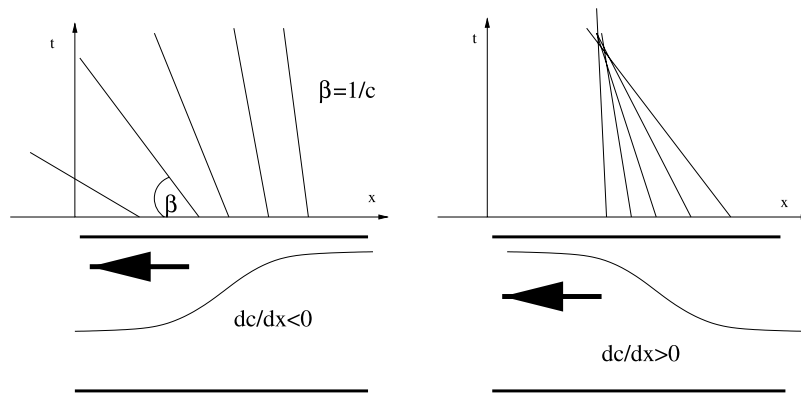
Figure B1. Schematic view of the characteristics emanating from a (left) rarefacting and (right) steepening wave. In the former case, characteristics fan out and never intersect. In the latter, the characteristics intersect after a finite time. When this happens, a shock (discontinuity) develops and the hydrostatic model breaks down.

where c_i are the characteristic speeds. For purpose of discussion, let $N = 1$. Thus, to obtain the solution at location $(\mathbf{x}, t)$, it is necessary to backtrack along the characteristics until $t = 0$ is reached at location x_0. The value of the Riemann invariants based on the initial condition at x_0 determines the value of the solution at $(\mathbf{x}, t)$. Unless the propagation media is non dispersive and the equations are linear, the characteristic speeds are not uniform. Figure B1 shows a schematic view of the characteristics emanating from a traveling wave governed by equation (8). For simplicity, only one set of characteristics is shown. On the left side, c increases in the direction of propagation of the wave. Thus the characteristics fan out and the solution is well defined at all times. On the right side, the speed of the characteristics decreases in the direction of propagation, leading to the intersection of characteristics emanating from different points of the initial condition. When this happens, the solution generates a discontinuity (a shock) and the solution breaks down in the vicinity of the shock. The solution to this problem is to realize that as the solution becomes steeper and steeper, dispersive effects (not included in the hydrostatic model) become important and the problem ceases to be hyperbolic. Note that away from shocks, the solution still satisfies the hyperbolic (hydrostatic) limit. If appropriate ways of merging the left and right side of the discontinuity can be applied ("shock" conditions), then the hydrostatic model can still be applied after the shock forms. It is clear how knowledge of c can be used to diagnose the potential onset of discontinuities.

References

Ablowitz, M. J., and H. Segur (1981), *Solitons and the Inverse Scattering Transform*, Soc. for Indust. and Appl. Math, Philadelphia, Pa.

Abramowitz, M., and I. A. Stegun (1964), *Handbook of Mathematical Functions with Formulas, Graphs, and Mathematical Tables*, Dover, New York.

Akylas, T. R., and K. S. Davis (2001), Three-dimensional aspects of non-linear stratified flow over topography near the hydrostatic limit, *J. Fluid Mech.*, *428*, 81–105.

Apel, J. R. (2003), A new analytical model for internal solitons in the oceans, *J. Phys. Oceanogr.*, *33*, 2247–2269.

Apel, J. R., J. R. Holbrook, J. Tsai, and A. K. Liu (1985), The Sulu Sea internal soliton experiment, *J. Phys. Oceanogr.*, *15*, 1625.

Apel, J. R., L. A. Ostrovsky, and Y. A. Stepanyants (1995), Internal solitons in the ocean, *Tech. Rep. MERCJRA0695*, Appl. Phys. Lab., Johns Hopkins Univ., Baltimore, Md.

Baines, P. G. (1995), *Topographic Effects in Stratified Flows*, Cambridge Univ. Press, New York.

Benney, D. J. (1966), Long nonlinear waves in fluid flows, *J. Math. Phys.*, *45*, 52–63.

Bogucki, D., T. Dickey, and L. F. Redekopp (1997), Sediment resuspension and mixing by resonantly generated internal solitary waves, *J. Phys. Oceanogr.*, *27*, 1181.

Bourgalt, D., D. E. Kelley, and P. Galbraith (2005), Interfacial solitary wave run-up in the St. Lawrence estuary, *J. Mar. Res.*, *63*, 1001–1015.

Brandt, P., W. Alpers, and J. O. Backhaus (1996), Study of the generation and propagation of internal waves in the Strait of Gibraltar using a numerical model and synthetic aperture radar images of the European ERS-1 satellite, *J. Geophys. Res.*, *101*, 14,237–14,252.

Butman, B., P. S. Alexander, S. P. Anderson, F. L. Lightsom, A. Scotti, and R. C. Beardsley (2004), The Massachusetts Bay Internal Wave Experiment, August 1998: Data report, *Data Ser. 85*, U.S. Geol. Surv., Woods Hole, Mass.

Butman, B., P. S. Alexander, A. Scotti, R. C. Beardsley, and S. Anderson (2006), Large internal waves in Massachusetts Bay transport sediment offshore, *Cont. Shelf. Res.*, *26*(17–18), 2029–2049.

Canuto, C., M. Y. Hussaini, A. Quarteroni, and T. A. Zang (1987), *Spectral Methods in Fluid Dynamics*, Springer, New York.

Chereskin, T. K. (1983), Generation of internal waves in Massachusets Bay, *J. Geophys. Res.*, *88*, 2649–2661.

Choi, W., and R. Camassa (1999), Fully nonlinear internal waves in a two-fluid system, *J. Fluid Mech.*, *396*, 1–36.

Colosi, J. A., R. C. Beardsley, J. F. Lynch, G. Gawarkiewicz, C.-S. Chiu, and A. Scotti (2001), Observation of nonlinear internal waves on the New England continental shelf during Summer Shelfbreak Primer study, *J. Geophys. Res.*, *106*, 9587–9601.

Courant, R., and D. Hilbert (1989), *Method of Mathematical Physics*, vol. 2, Wiley-Intersci., Hoboken, N. J.

Cummins, P. F. (2000), Stratified flow over topography: Time-dependent comparisons between model solutions and observations, *Dyn. Atmos. Ocean*, *33*, 43–72.

Farmer, D., and L. Armi (1998), Stratified flow over topography: The role of small-scale entrainment and mixing in flow establishment, *Proc. R. Soc., Ser. A*, *455*, 3221–3258.

Farmer, D., and L. Armi (1999), The generation and trapping of solitary waves over topography, *Science*, *283*, 188–190.

Fornberg, B. (1984), A numerical method for conformal mapping of doubly connected regions, *SIAM J. Sci Stat. Comput.*, *5*, 771–783.

Fu, L.-L., and B. Holt (1984), Internal waves in the Gulf of California: Observations from a space-borne radar, *J. Geophys. Res.*, *89*, 2053.

Greenberg, D. A. (1979), A numerical model investigation of tidal phenomena in the Bay of Fundy and Gulf of Maine, *Mar. Geod.*, *2*, 161–187.

Grimshaw, R. H. J., and N. Smyth (1986), Resonant flow of a stratified fluid over topography, *J. Fluid Mech.*, *169*, 429–464.

Grimshaw, R., E. Pelinovsky, and T. Talipova (1999), Solitary wave transformation in a medium with sign-variable quadratic nonlinearity and cubic nonlinearity, *Physica D*, *132*, 40–62.

Gurevich, A. V., and L. P. Pitaevskii (1973a), Decay of initial discontinuity in the Korteweg-de Vries equation, *Sov. Phys. JETP Lett., Engl. Transl.*, *17*, 193–195.

Gurevich, A. V., and L. P. Pitaevskii (1973b), Nonstationary structure of a collisionless shock wave, *Zh. Eksp. Teor. Fiz.*, *65*(2), 590–604.

Halpern, D. (1971a), Semidiurnal tides in Massachusetts Bay, *J. Geophys. Res.*, *76*, 6573–6584.

Halpern, D. (1971b), Observations on short-period internal waves in Massachusetts Bay, *J. Mar. Res.*, *29*, 116–132.

Haury, L. H., M. G. Briscoe, and M. H. Orr (1979), Tidally generated internal wave packets in Massachusetts Bay, *Nature*, *278*, 312–317.

Haury, L. H., P. H. Wiebe, M. H. Orr, and M. B. Briscoe (1983), Tidally generated high frequency internal wave packets and their effects on plankton in Massachusetts Bay, *J. Mar. Res.*, *41*, 65–112.

Helfrich, K. (2007), Decay and return of internal solitary waves with rotation, *Phys. Fluids*, *19*, 026601, doi:10.1063/1.2472509.

Helfrich, K. R., and W. K. Melville (2006), Long nonlinear internal waves, *Ann. Rev. Fluid Mech.*, *38*, 395–425.

Helfrich, K. R., and J. Pineda (2003), Accumulation of particles in propagating fronts, *Limnol. Oceanogr.*, *48*, 1509–1520.

Hibiya, T. (1988), The generation of internal waves by tidal flow over Stellwagen Bank, *J. Geophys. Res.*, *93*, 533–542.

Holloway, P. E., E. Pelinovsky, T. Talipova, and B. Barnes (1997), A nonlinear model of internal tide transformation on the Australian north west shelf, *J. Phys. Oceanogr.*, *27*, 871–896.

Holloway, P. E., E. Pelinovsky, and T. Talipova (1999), A generalized Korteweg-de Vries model of internal tide transformation in the coastal zone, *J. Geophys. Res.*, *104*, 18,333–18,350.

Holt, J. T., and S. A. Thorpe (1997), The propagation of high-frequency internal waves in the Celtic Sea, *Deep Sea Res., Part I*, *44*, 2087–2116.

Jackson, C. R. (2004), *An Atlas of Internal Solitary-like Internal Waves*, Global Ocean Assoc., Alexandria, Va.

Joseph, R. J. (1977), Solitary waves in a finite depth fluid, *J. Phys. A Math Gen.*, *10*, L225–L227.

Korteweg, D. J., and G. de Vries (1895), On the change of form of long waves advancing in a rectangular canal, and on a new type of long stationary waves, *Philos. Mag.*, *39*, 422–443.

Lamb, K. (1994), Numerical experiments of internal wave generation by strong tidal flow across a finite-amplitude bank edge, *J. Geophys. Res.*, *99*, 843–864.

Lamb, K. (1997), Particle transport by non-breaking, solitary internal waves, *J. Geophys. Res.*, *102*, 18,641–18,660.

Lamb, K. (2007), Energy and pseudoenergy flux in the internal wave field generated by tidal flow over topography, *Cont. Shelf Res.*, *27*(9), 1208–1232.

Lee, C.-Y., and R. C. Beardsley (1974), The generation of long nonlinear internal waves in weakly stratified shear flows, *J. Geophys. Res.*, *79*, 453–462.

Leichter, J. J., H. L. Stewart, and S. L. Miller (2003), Episodic nutrient transport of Florida coral reefs, *Limnol. Oceanogr.*, *48*, 1394–1407.

Liu, A. K. (1988), Analysis of nonlinear internal waves in the New York Bight, *J. Geophys. Res.*, *93*, 12,317–12,329.

Liu, A. K., and D. J. Benney (1981), The evolution of nonlinear wave trains in stratified shear flows, *J. Phys. Oceanogr.*, *15*, 1613–1624.

MacKinnon, J., and M. Gregg (2003), Mixing on the late-summer New England shelf—Solibores, shear and stratification, *J. Phys. Oceanogr.*, *33*, 1476–1492.

Marshall, J., C. Hill, L. Perelman, and A. Adcroft (1997), Hydrostatic, quasi-hydrostatic, and nonhydrostatic ocean modeling, *J. Geophys. Res.*, *102*, 5733–5752.

Moum, J. N., D. M. Farmer, W. D. Smyth, L. Armi, and S. Vagle (2003), Structure and generation of turbulence at interfaces strained by internal solitary waves propagating shoreward over the continental shelf, *J. Phys. Oceanogr.*, *33*, 2093–2112.

New, A. L., and R. D. Pingree (1992), Local generation of internal soliton packets in the central Bay of Biscay, *Deep Sea Res.*, *39*, 1521–1534.

Ono, H. (1975), Algebraic solitary waves in stratified fluids, *J. Phys. Soc. Jpn.*, *39*, 1082–1091.

Osborne, A. R., and T. I. Burch (1980), Internal solitons in the Andaman Sea, *Science*, *208*, 451–460.

Ostrovsky, L. A., and J. Grue (2003), Evolution equations for strongly nonlinear internal waves, *Phys. Fluids*, *15*, 2934–2948.

Pawlack, G., and L. Armi (1998), Vortex dynamics in a spatially accelerating shear layer, *J. Fluid Mech.*, *376*, 1–35.

Pineda, J. (1999), Circulation and larval distribution in internal tidal bore warm fronts, *Limnol. Oceanogr.*, *44*, 1400–1414.

Ramp, S. R., T. Y. Tang, T. F. Duda, J. F. Lynch, A. K. Liu, C.-S. Chiu, F. L. Bahr, H.-R. Kim, and Y.-J. Yang (2004), Internal solitons in the northeastern South China Sea Part I: Sources and deep water propagation, *IEEE J. Ocean. Eng.*, *29*, 1157–1181.

Sandstrom, H., and J. A. Elliot (1984), Internal tide and solitons on the Scotian Shelf, *J. Geophys Res.*, *89*, 6415–6426.

Scotti, A., and J. Pineda (2007), Plankton accumulation and transport in propagating nonlinear internal fronts, *J. Mar. Res.*, *65*, 117–145.

Scotti, A., R. Beardsley, and B. Butman (2006), On the interpretation of energy and energy fluxes of nonlinear internal waves: An example from Massachusetts Bay, *J. Fluid Mech.*, *561*, 103–112.

Small, J. (2003), The refraction and shoaling of non-linear internal waves at the Malin shelf break, *J. Phys. Oceanogr.*, *33*, 2657–2674.

Small, J., T. C. Sawyer, and J. C. Scott (1999), The evolution of an internal bore at the Malin shelf break, *Ann. Geophys.*, *17*, 547–565.

Smith, R. B. (1985), On severe downslope winds, *J. Atmos. Sci.*, *42*, 2597–2603.

Smyth, N. F., and P. E. Holloway (1988), Hydraulic jump and undular bore formation on a shelf break, *J. Phys. Oceanogr.*, *18*, 947–962.

Stanton, T. P., and L. A. Ostrovsky (1998), Observations of highly nonlinear, tidally forced solitons over the continental shelf, *Geophys. Res. Lett.*, *25*, 2695–2698.

Trask, R. P., and M. G. Briscoe (1983), Detection of Massachusetts Bay internal waves by the synthetic aperture radar (SAR) on SEASAT, *J. Geophys. Res.*, *88*, 1789–1799.

Trevorrow, M. V. (1998), Observations of internal solitary waves near the Oregon coast with an inverted echo sounder, *J. Geophys. Res.*, *103*, 7671–7680.

Vlasenko, V., and K. Hutter (2002), Numerical experiments of the breaking of solitary internal waves over a slope-shelf topography, *J. Phys. Oceanogr.*, *32*, 1779–1793.

Whitham, G. B. (1974), *Linear and Nonlinear Waves*, Wiley-Intersci., Hoboken, N. J.

Ziegenbein, J. (1969), Short internal waves in the Strait of Gibraltar, *Deep Sea Res.*, *16*, 479–487.

————————————

R. C. Beardsley, Department of Physical Oceanography, Woods Hole Oceanography Institution, Woods Hole, MA 02543, USA. (rbeardsley@whoi.edu)

B. Butman, U. S. Geological Survey, Woods Hole, MA 02543, USA. (bbutman@whoi.edu)

A. Scotti, Department of Marine Sciences, University of North Carolina, Chapel Hill, NC 27599, USA. (ascotti@unc.edu)